Transdimensional ambient-noise surface wave tomography of the Reykjanes Peninsula, SW Iceland

Rahimi Dalkhani, Amin; Áústsdóttir, Thorbjörg; Gudnason, Egill Árni; Hersir, Gylfi Páll; Zhang, Xin; Weemstra, Cornelis

DOI
10.1093/gji/ggad435

Publication date
2023

Document Version
Final published version

Published in
Geophysical Journal International

Geophysical Journal International

Geophys. J. Int. (2024) **236,** 621–643
Advance Access publication 2023 November 2
GJI Seismology

https://doi.org/10.1093/gji/ggad435

Transdimensional ambient-noise surface wave tomography of the Reykjanes Peninsula, SW Iceland

Amin Rahimi Dalkhani,[1] Thorbjörg Áústsdóttir,[2] Egill Árni Gudnason,[2] Gylfi Páll Hersir,[3] Xin Zhang [4,5] and Cornelis Weemstra [1,6]

[1] *Department of Geoscience and Engineering, Delft University of Technology,* 2628 *CN Delft, The Netherlands. E-mail: a.rahimidalkhani@tudelft.nl*
[2] *Iceland GeoSurvey (ÍSOR Urðrhvarf* 8, 203 *Kópavogur, Kt.* 600503-4050, *Iceland*
[3] *Independent researcher, Reykjavík, Iceland*
[4] *School of Geosciences, College of Science and Engineering, University of Edinburgh, Edinburgh EH*8 9*YL, Scotland*
[5] *School of Earth Sciences and Resources, School of Engineering and Technology, China University of Geosciences, Haidian District,* 100190 *Beijing, China*
[6] *Seismology and Acoustics, Royal Netherlands Meteorological Institute,* 3731 *GA De Bilt, The Netherlands*

Accepted 2023 October 31. Received 2023 October 31; in original form 2023 February 20

SUMMARY

Ambient noise seismic tomography has proven to be an effective tool for subsurface imaging, particularly in volcanic regions such as the Reykjanes Peninsula (RP), SW Iceland, where ambient seismic noise is ideal with isotropic illumination. The primary purpose of this study is to obtain a reliable shear wave velocity model of the RP, to get a better understanding of the subsurface structure of the RP and how it relates to other geoscientific results. This is the first tomographic model of the RP which is based on both on- and off-shore seismic stations. We use the ambient seismic noise data and apply a novel algorithm called one-step 3-D transdimensional tomography. The main geological structures in the study area (i.e. covered by seismic stations) are the four NE–SW trending volcanic systems, orientated highly oblique to the plate spreading on the RP. These are from west to east; Reykjanes, Eldvörp-Svartsengi, Fagradalsfjall and Krýsuvík, of which all except Fagradalsfjall host a known high-temperature geothermal field. Using surface waves retrieved from ambient noise recordings, we recovered a 3-D model of shear wave velocity. We observe low-velocity anomalies below these known high-temperature fields. The observed low-velocity anomalies below Reykjanes and Eldvörp-Svartsengi are significant but relatively small. The low-velocity anomaly observed below Krýsuvík is both larger and stronger, oriented near-perpendicular to the volcanic system, and coinciding well with a previously found low-resistivity anomaly. A low-velocity anomaly in the depth range of 5–8 km extends horizontally along the whole RP, but below the high-temperature fields, the onset of the velocity decrease is shallower, at around 3 km depth. This is in good agreement with the brittle–ductile transition zone on the RP. In considerably greater detail, our results confirm previous tomographic models obtained in the area. This study demonstrates the potential of the entirely data-driven, one-step 3-D transdimensional ambient noise tomography as a routine tomography tool and a complementary seismological tool for geothermal exploration, providing an enhanced understanding of the upper crustal structure of the RP.

Key words: Interferometry; Tomography; Seismic noise; Surface waves and free oscillations.

1 INTRODUCTION

The Reykjanes Peninsula (RP), southwest Iceland, is the onshore continuation of the Mid-Atlantic Ridge. As such, it is part of the divergent plate boundary of the North American and Eurasian plates. On the RP, this plate boundary strikes N70°E (Sigmundsson *et al.* 2020), and the divergence of the plates is expressed in six en-echelon rift segments, which accommodate the rifting (Sæmundsson *et al.* 2020). These rift segments, or volcanic systems, are areas with the highest density of eruptive fissures and tectonic faults and fractures. Currently, there are two geothermal power plants in production on the RP, that is in Reykjanes (100 MWe) and Svartsengi (76 MWe and 150 MWt), mainly producing from depths of 1–2.5 km (Fig. 1; Friðleifsson *et al.* 2020).

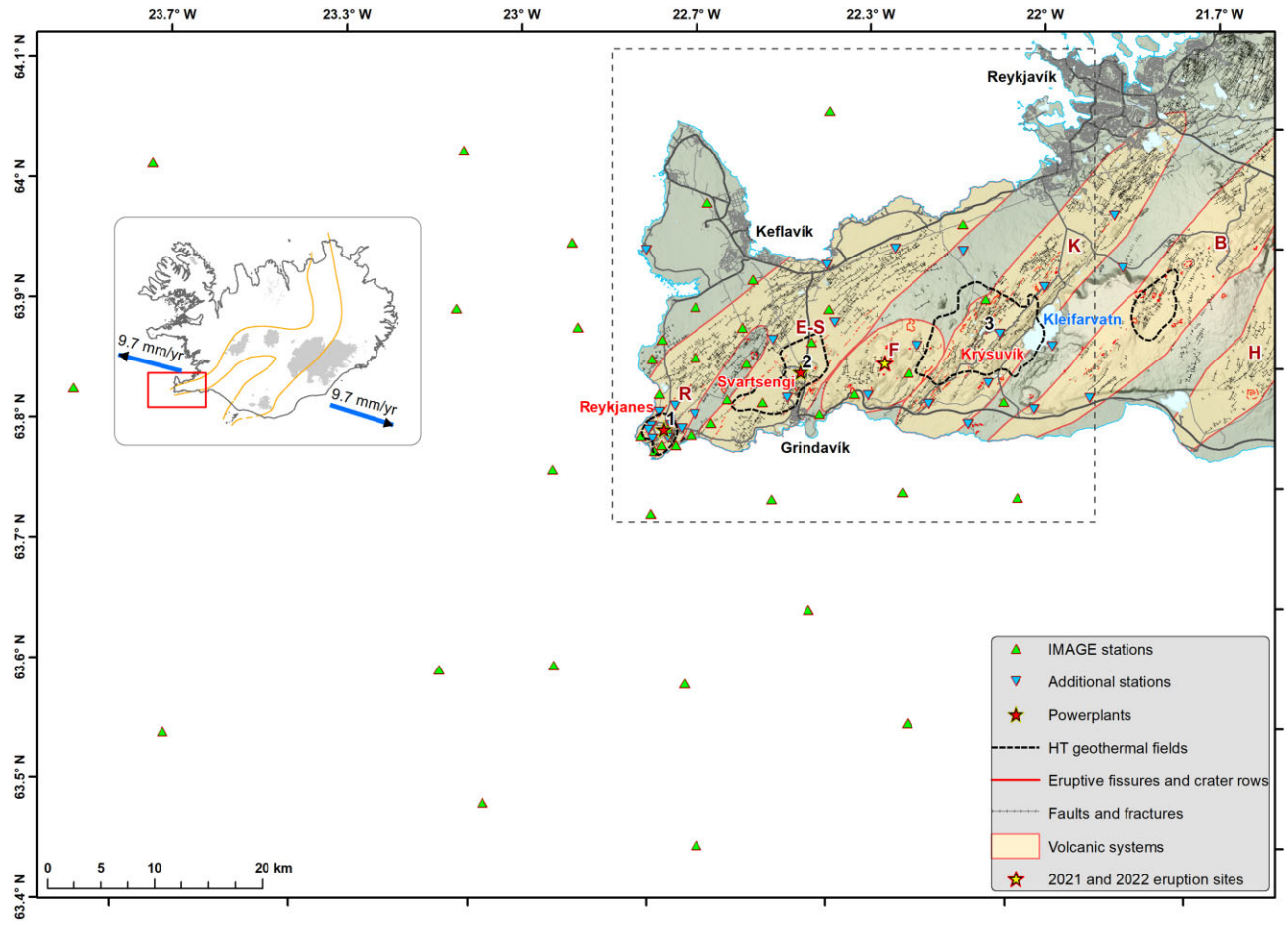

Figure 1. The seismic network and the geological setting of the study area. Green triangles are IMAGE seismic stations (both on- and off-shore). Blue inverted triangles are additional seismic stations from other existing seismic networks in the area. Red and black fault lines denote postglacial volcanic eruptive and opening fissures, respectively; the volcanic systems are shaded light brown and marked with a bold letter, R: Reykjanes, E-S: Eldvörp-Svartsengi, F: Fagradalsfjall, K: Krýsuvík, B: Brennisteinsfjöll, H: Hengill (Sæmundsson & Sigurgeirsson 2013); black dashed polygons show the extent of the high-temperature geothermal fields on the Peninsula according to resistivity measurements (summarized in Flóvenz *et al.* 2022) and the geothermal power plants of Svartsengi and Reykjanes are shown with red stars. The approximate location of the 2021 and 2022 Fagradalsfjall eruptions (Pedersen *et al.* 2022), as well as the 2023 eruption, is shown with a yellow star. The black-dashed rectangle shows the map extent of Fig. 5. Main roads are in black, and main landmarks referenced in the text are shown on the map. The inset shows volcanic zones of Iceland (orange) with blue arrows indicating the plate spreading rate in Iceland (Sigmundsson *et al.* 2020). The red rectangle on the inset shows the location of the zoomed-in area.

Further exploration of deep geothermal resources is currently underway. In 2016–2017, a deep exploratory well (IDDP-2) was drilled down to a depth of 4.6 km in Reykjanes to examine the economic potential of the production of supercritical fluids from greater depths than conventional production wells. The IDDP-2 well reached both supercritical conditions, evidenced by a temperature estimated to be around 600 °C at the bottom of the well (Bali *et al.* 2020), and permeability at depths greater than 3 km, evidenced by a total loss of circulation below 3 km during drilling. In addition, seismicity was induced below 3 km, in a zone that was generally aseismic prior to drilling (Gudnason *et al.* 2020; Friðleifsson *et al.* 2020). For further geothermal utilization, more investigation is needed to better understand the crustal structure beneath the RP as a whole.

The RP has been the subject of several different geological (Clifton & Kattenhorn 2006; Sæmundsson & Sigurgeirsson 2013; Sæmundsson *et al.* 2020) and geophysical studies. See Jousset *et al.* (2020b) for an exhaustive list of recent geophysical studies. In particular, the recent volcano-tectonic unrest period at Fagradalsfjall and the subsequent eruptions in 2021, 2022 and 2023 (the first eruptions on the RP in roughly 780 yr) have drawn Fagradalsfjall and the RP as a whole into the spotlight (Flóvenz *et al.* 2022; Halldórsson *et al.* 2022; Pedersen *et al.* 2022; Sigmundsson *et al.* 2022; Einarsson *et al.* 2023). Relatively high-resolution shear wave images have the potential to reveal more details of the RP's subsurface in general and the volcanic systems in particular. Ambient noise surface wave tomography (ANSWT) has great potential in this context (e.g. Lehujeur *et al.* 2016; Zhang *et al.* 2020). This is due to (i) the 3-D shear wave images it can provide in the absence of active seismic sources, (ii) its relatively low costs, supplementary to a local seismic network and (iii) the considerable investigation depth it can reach, compared to many other geophysical methods (Cruz-Hernández *et al.* 2022).

Jousset *et al.* (2016) used recordings by 26 seismic stations on the RP to retrieve both surface and body waves. The seismic stations used by Jousset *et al.* (2016) constitute a subset of the IMAGE seismic network (for details regarding the IMAGE project we refer to Hersir *et al.* 2020b; Blanck *et al.* 2020). Martins *et al.* (2020) used the noise recorded by (almost) the same subset as Jousset *et al.* (2016) to image part of the RP by means of deterministic ANSWT.

Even though their findings enhanced details compared to previous models, the resolution and lateral extent of the obtained images are limited. Both studies used a subset of the IMAGE stations because the recordings by the Ocean Bottom Seismometers (OBSs; also deployed in the context of IMAGE) were subject to clock drift. In addition, the IMAGE seismic network was extended with stations from other existing seismic networks on the RP. We henceforth refer to the combined set of stations as the 'extended IMAGE seismic network' (i.e. the IMAGE stations complimented with additional stations from the existing seismic networks; see Section 3 for further details). The recordings by some of the additional stations of the existing networks also turned out to be subject to timing errors in the frequency band of interest. Weemstra *et al.* (2021) quantified both the average clock drift by most of the OBSs and the timing errors of most of the stations of the existing seismic networks. Removal of the recovered timing errors allows those recordings to be used for ANSWT. This significantly increases lateral extent and resolution compared to Jousset *et al.* (2016) and Martins *et al.* (2020). We finally highlight that what is referred to as the extended IMAGE seismic network in this study, is referred to as the Reykjanes array (RARR) in Weemstra *et al.* (2021) and Rahimi Dalkhani *et al.* (2021).

In this study, we use a recently developed probabilistic tomographic algorithm (Zhang *et al.* 2018, 2020; Rahimi Dalkhani *et al.* 2021) to perform ANSWT of the RP. The shear wave velocities obtained in this study result from a 3-D, one-step Bayesian tomographic inversion (Zhang *et al.* 2018), which has its roots in the transdimensional inversion algorithm introduced by Bodin & Sambridge (2009). Rahimi Dalkhani *et al.* (2021) modified the algorithm in the sense that they update the ray paths less frequently (i.e. not at every perturbation step), while at the same time still honouring the non-linear aspect of the tomographic problem. They tested the modified algorithm on synthetic station–station traveltimes generated for the configuration of the extended IMAGE seismic network and the surface wave frequencies of interest (i.e. 0.1–0.5 Hz). In this study, we apply the modified algorithm to the extended IMAGE data set. First, we retrieve station–station surface wave phase traveltimes from the time-corrected ambient noise recordings (Weemstra *et al.* 2021). Then, we use these surface waves' dispersion curves to generate 3-D images of the RP subsurface' shear wave velocity. Finally, we interpret the recovered shear wave velocities, discuss how they compare to other recent geophysical studies, and list the most important conclusions.

2 GEOLOGICAL SETTING

The tectonic structure of the RP is characterized by six volcanic systems, arranged en-echelon along the divergent plate boundary of the North American and Eurasian plates. On the RP, this plate boundary is approximately 60 km long, from the SW tip of the Peninsula, until it joins the Western Volcanic Zone and the South Iceland Seismic Zone at the Hengill triple junction in the east. The RP oblique rift is expressed by a 5–10 km wide seismic and volcanic zone along the Peninsula, and is highly oblique with the spreading direction of N120°E in this region (Sigmundsson *et al.* 2020; Sæmundsson *et al.* 2020). Four of the six identified volcanic systems of the RP are within our area of study (all six are shown in Fig. 1 as shaded light brown polygons).

The volcanic systems on the RP are grouped by the presence of eruptive fissures and the density of tectonic faults and fractures. Their outlines or boundaries are rough estimates, drawn according to Sæmundsson & Sigurgeirsson (2013). During the last RP rifting episode, *ca*. 1200–780 yr before present, all the RP's volcanic systems were volcanically active in intervals, except Fagradalsfjall and Hengill (Sæmundsson & Sigurgeirsson 2013). The extensional component of the rifting is accommodated by the intrusion of magma in NE–SW oriented dykes, oblique to the plate boundary. The remaining strike-slip component of the rifting is accommodated by N–S oriented strike-slip faults, which are known to be capable of producing earthquakes of moment magnitude as high as 6 (Einarsson 1991; Björnsson *et al.* 2020). The volcanic systems (Fig. 1) are from west to east: (1) Reykjanes, (2) Eldvörp-Svartsengi, (3) Fagradalsfjall, (4) Krýsuvík, (5) Brennisteinsfjöll and (6) Hengill. All, except Fagradalsfjall, comprise a known high-temperature (HT) geothermal field (black dashed polygons in Fig. 1). The HT polygons show the extent of the geothermal fields, according to resistivity values at 1 km depth (Flóvenz *et al.* 2022, and references therein). Both the Eldvörp-Svartsengi and Reykjanes HT fields host an operating geothermal power plant. It is worth noting that Eldvörp is a subfield of Svartsengi, and as such, Eldvörp is included in the resistivity outline of Svartsengi.

The upper crustal structure of the RP is built of extrusive basaltic rocks with a downward-increasing alteration and a greater proportion of intrusive rocks. The upper crust is roughly 4.5 km thick on the RP (Pálmason 1971; Flóvenz *et al.* 1980; Weir *et al.* 2001). It is believed that intrusive rocks build the lower crust down to Moho, which is located at a depth of around 15 km (Weir *et al.* 2001). The brittle–ductile transition (BDT) zone, with an estimated temperature of around 600 °C in basaltic rocks (Ágústsson & Flóvenz 2005; Violay *et al.* 2012), is typically located at 6–7 km depth beneath the RP and rises up to 3–5 km depth below the HT fields (Blanck *et al.* 2020; Gudnason *et al.* 2020; Flóvenz *et al.* 2022). Crustal thickening along the RP from west to east is observed both by wide-angle reflection seismic (Weir *et al.* 2001) and local earthquake tomography (Tryggvason *et al.* 2002).

3 ACQUISITION AND DATA

As a part of IMAGE (Integrated Methods for Advanced Geothermal Exploration; Hersir *et al.* 2020b), a dense seismic network was installed on and around the RP in 2014 (Jousset *et al.* 2020a; Blanck *et al.* 2020). It consisted of 30 on-land stations and 24 OBSs. In addition to this temporary IMAGE network, data from other existing seismic networks in the area were made available to the project. These were (i) a local monitoring network run by HS Orka/ÍSOR, (ii) REYKJANET (Horálek 2013) run by the Czech Academy of Science (CAS) in co-operation with ÍSOR on the central and eastern part of the Peninsula and (iii) permanent stations run by the Icelandic Meteorological Office (IMO; Icelandic Meteorological Office 1992; Jakobsdóttir 2008). Results based on the seismic data from the 30 onshore stations of the IMAGE network have been published by, for example Jousset *et al.* (2016), Verdel *et al.* (2016), Weemstra *et al.* (2016) and Martins *et al.* (2020). In this study, we use the recordings by all four seismic networks (i.e. blue and green triangles in Fig. 1), whose combination we refer to as the 'extended IMAGE seismic network'.

The extended IMAGE seismic network sampled the seismic noise field between April 2014 and August 2015 using a total of 83 seismic stations. Weemstra *et al.* (2016) computed the surface wave responses (i.e. time-averaged cross-correlation functions) from the recorded ambient noise data. However, many of the stations turned out to be subject to timing errors. Consequently, Martins *et al.* (2020) used a subset of the stations (the ones without the timing errors: 30 onshore seismometers of the IMAGE seismic network)

in a two-step linearized ANSWT algorithm. Then, Weemstra *et al.* (2021) recovered the timing errors for most of the additional stations, subsequently allowing them to also correct the computed cross-correlation functions. Time-averaged cross-correlations associated with four of the 83 stations had to be discarded after all. This was due to an unrecoverable timing error (one station; O20; see Weemstra *et al.* 2021), and insufficient noise recordings (three stations; VSV, O12 and O05; see fig. 1 of the supplementary materials of Weemstra *et al.* 2021). The active stations are depicted in Fig. 1 by green triangles. See Weemstra *et al.* (2021) for more details regarding seismic instruments and network characteristics. We only used vertical component recordings, because these are best suited for recovering Rayleigh waves; in particular in such a heterogeneous area (e.g. Haney *et al.* 2012).

Fig. 2 shows the interferometric responses of the extended IMAGE seismic network for the vertical components of the seismometers. The term interferometric is derived from 'seismic interferometry', which refers to the process of retrieving Green's function estimates from recordings of ambient seismic noise (Wapenaar & Fokkema 2006). The interferometric responses are the result of time-averaged cross-correlations of the recorded noise between the station couples. For the processing steps applied to the raw (noise) data to retrieve the interferometric responses, we refer to Weemstra *et al.* (2021). Similar to Weemstra *et al.* (2021) and Martins *et al.* (2020), we focus on surface waves in the 0.1–0.5 Hz frequency range, which give the most reliable results.

We retrieve the frequency-dependent phase velocities from the interferometric responses computed and corrected by Weemstra *et al.* (2021) for each station couple, by calculating and picking the most sensible zero-crossings (e.g. Ekström *et al.* 2009; Kästle *et al.* 2016; Lindner *et al.* 2018). Details are provided in Appendix A. The picked phase velocities are then converted to the frequency-dependent phase traveltimes, which are inverted for shear wave velocities using the one-step transdimensional algorithm (Zhang *et al.* 2018; Rahimi Dalkhani *et al.* 2021).

4 INTERFEROMETRIC TRAVELTIMES

We extract phase velocity dispersion curves from the interferometric responses (station–station time-averaged cross-correlations; see Fig. 2). The procedure, algorithm and criteria are explained and exemplified in Appendix A. Fig. 3(a) shows all the picked dispersion curves as blue dotted lines. The mean phase velocity, and curves representing two, and three standard deviations (calculated separately at each frequency) are depicted as black, green and red lines, respectively. After a careful analysis of these dispersion curves, we decided to discard dispersion curves whose velocity deviates more than three standard deviations from the mean. This analysis involved evaluating the spatial distribution of the station couples associated with dispersion curves whose velocity exceeded two standard deviations (following Schippkus *et al.* 2018). By simply displaying the corresponding rays (with the phase velocity colour-coded; see Fig. S1), we find that the discarded station couples are concentrated in a specific area, which coincides with an area traversed by rays that exhibit (anomalously) low shear wave velocities (resulting from an inversion with the retained dispersion curves; i.e. within two standard deviations of the mean). In other words, there is no random pattern in the spatial distribution of the outliers. Also, the Fig. S1 reveals that it is not a single station that is a source of error. This suggests that the discarded dispersion curves are merely representative of the velocity structure in the area. It is therefore that we retain all dispersion curves that are within three standard deviations of the mean. We hence discard a limited number of station–station cross-correlations.

The number of retained phase velocity measurements per frequency is depicted in Fig. 3(b). Note the variation between different frequencies is predominantly to (i) the decreasing SNR with increasing frequency (and hence the picking being terminated by the picking algorithm) and (ii) the increasing number of station couples exceeding the aforementioned condition that the station–station distance needs to exceed one and a half wavelength. The most sensitive depth is also depicted for each period by means of a red stem plot in Fig. 3(b). As a rule of thumb, fundamental-mode Rayleigh waves are most sensitive to the shear wave speed at depths around one-third ($\frac{1}{3}$) of their corresponding wavelength (Fang *et al.* 2015; Rahimi Dalkhani *et al.* 2021), where the corresponding wavelength at each period is computed based on the mean dispersion curve (black curve in Fig. 3a).

Fig. 3(b) shows that the retrieved surface waves are most sensitive to structures with a depth of 2–8 km [sensitivity kernels are explicitly computed for a few characteristic phase velocity functions with depth in Rahimi Dalkhani *et al.* (2021)]. This implies that (small-scale) structures near the surface (shallower than 2 km) are not expected to be resolved very well. To reveal more details of the near-surface, higher frequencies would need to be included in the inversion. Potential residual timing errors (Weemstra *et al.* 2021), lower SNRS, and interference of higher modes did not allow us to extract reliable fundamental-mode phase velocities at frequencies beyond 0.5 Hz [let alone potential cross-modal terms obscuring the time-averaged cross-correlations; Halliday & Curtis (2008)].

Figs 3(c) and (d) shows the eligible station couples as straight rays at two different frequencies. The colour of the rays indicates the picked phase velocity for that station couple at that frequency. Note that some structures (in terms of shear wave velocity) can already be inferred from Figs 3(c) and (d). For the purpose of the 3-D (McMC) tomographic inversion, frequency-dependent phase velocities are converted to frequency-dependent traveltimes by dividing station–station distances by the phase velocities.

5 SURFACE WAVE TOMOGRAPHY

Once the frequency-dependent traveltimes are retrieved from all eligible interferometric responses and for all eligible discrete frequencies f_i, the data vector can be built. This data vector contains the frequency-dependent station–station traveltimes and serves as input to our probabilistic tomographic algorithm in order to recover the shear wave velocity structure of the subsurface. The core of every probabilistic algorithm is the forward function. In our context, this is a function that maps a known shear wave velocity distribution $v_s(x, y, z)$ to the data vector $\mathbf{d}$. Effectively, the forward process can be considered a two-step function:

$$v_s(x,y,z) \xrightarrow{F_1\left[v_s(x,y,z),f_i\right]} c_r(x,y,f_i) \xrightarrow{F_2\left[c_r(x,y,f_i),\mathbf{x}_k,\mathbf{x}_l\right]} \mathbf{d}(\mathbf{x}_k,\mathbf{x}_l,f_i), \quad (1)$$

where $v_s(x, y, z)$ is a known 3-D shear wave velocity model as a function of geographical location (x and y) and depth (z), $c_r(x, y, f_i)$ the frequency-dependent phase velocity as a function of x and y, and $\mathbf{d}(\mathbf{x}_k, \mathbf{x}_l, f_i)$ the data vector containing the station–station traveltimes for all station couples and eligible discrete frequencies f_i. Here, $\mathbf{x}_k$ and $\mathbf{x}_l$ are source and receiver locations ($k = l = 1, 2,..., N$, where N is the number of seismic stations). Similar to $c_r(x, y, f_i)$, these locations depend on x and y only as we ignore topography. The latter is justified by the fact that elevation differences in the area of

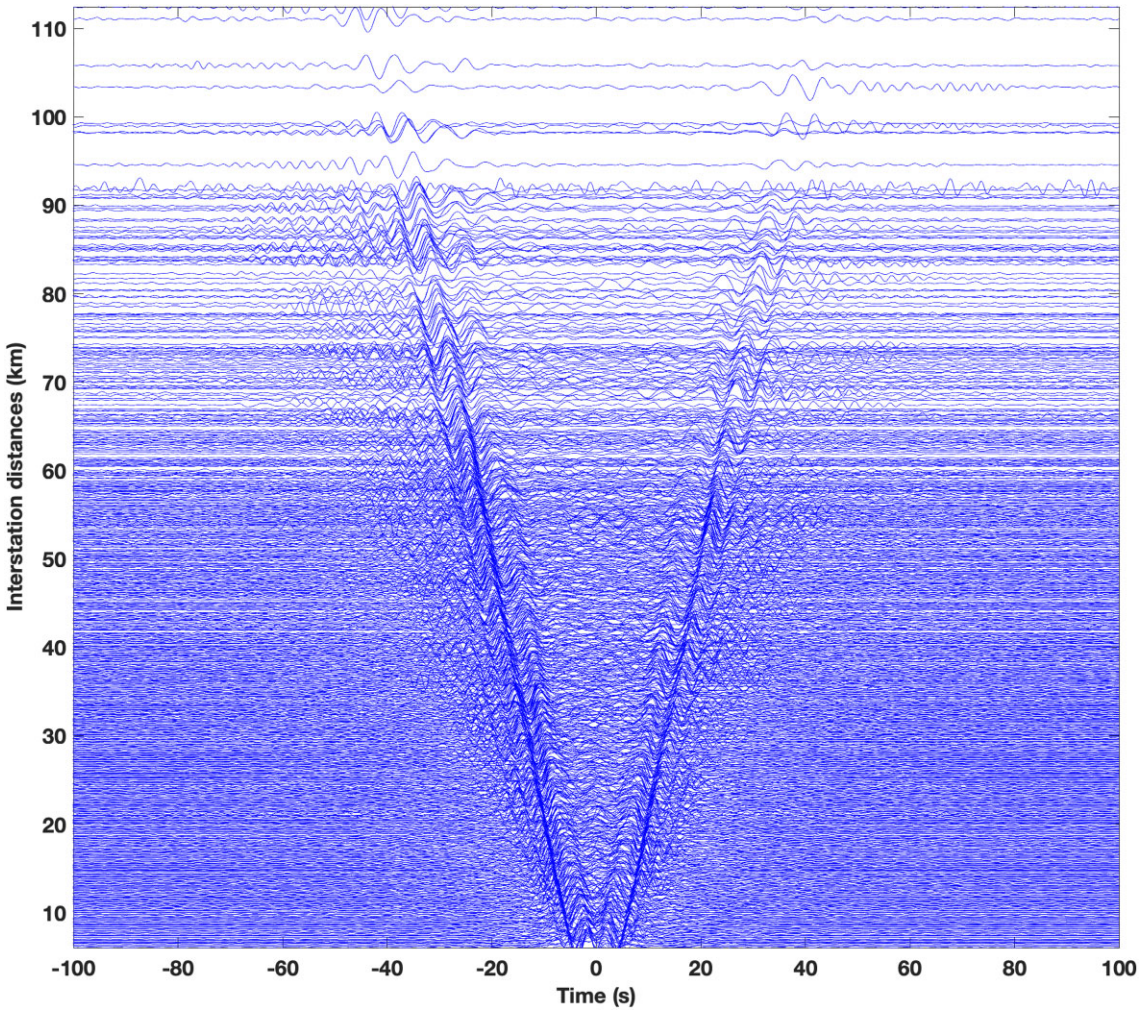

Figure 2. Time-averaged cross-correlations of recordings of ambient seismic noise filtered between 0.1 and 0.5 Hz. Cross-correlations are sorted by station–station distance and individually amplitude normalized. Showing all 79 stations used in the analysis.

interest do not exceed a few hundred meters, whereas the shortest wavelengths are in the order of 4 km (Rahimi Dalkhani *et al.* 2021). The data vector $\mathbf{d}(\mathbf{x}_k, \mathbf{x}_l, f_i)$ contains the frequency-dependent phase traveltimes depicted in Fig. 3. It is useful to note that $v_s(x, y, z)$ is often also referred to as a model vector $\mathbf{m}$ (Rahimi Dalkhani *et al.* 2021; Bodin & Sambridge 2009). Here, we should add that the *P*-wave velocity $v_p(x, y, z)$ is assumed to be a linear function of $v_s(x, y, z)$ according to $v_p = 1.78v_s$ (Allen *et al.* 2002) and that the mass density $\rho(x, y, z)$ is assumed to be related to the latter according to $\rho = 2.35 + 0.036(v_p - 3)^2$, where v_p and v_s are in km s^{-1} and ρ in g cm^{-3} (Kurita 1973; Zhang *et al.* 2020).

The function F_1 is the dispersion curve modelling algorithm (e.g. the modal approximation method of Herrmann 2013), whereas F_2 uses the fast marching method to solve the 2-D eikonal equation (e.g. Rawlinson & Sambridge 2004). This two-step forward function is the standard way to compute surface waves' frequency-dependent phase or group traveltimes. Similarly, a two-step process is commonly used to recover shear wave velocity structure from frequency-dependent traveltimes:

$$\mathbf{d}(\mathbf{x}_k, \mathbf{x}_l, f_i) \xrightarrow{F_2^{-1}\left[\mathbf{d}(\mathbf{x}_k, \mathbf{x}_l, f_i)\right]} c_r(x, y, f_i) \xrightarrow{F_1^{-1}\left[c_r(x, y, f_i)\right]} v_s(x, y, z). \quad (2)$$

First, a 2-D phase velocity map is recovered from the inversion of traveltimes at each frequency, F_2^{-1} (for different inversion methods see Rawlinson *et al.* 2003; Yao *et al.* 2006; Saygin & Kennett 2012; Bodin *et al.* 2012; Cabrera-Pérez *et al.* 2021). Then, the phase velocity maps are used together in a second inversion step, F_1^{-1}, to recover the shear wave velocity structure (e.g. Yao *et al.* 2008; Haney & Tsai 2015; Lehujeur *et al.* 2021). The two-step surface wave forward and inverse modelling are illustrated in the Figs S2(a)–(e) using a synthetic block model.

5.1 One-step transdimensional approach

The two-step inversion approach suffers from two issues. First, the initial 2-D inversion introduces (unknown) errors in the subsequent 1-D inversions. This is because usually only the mean and the standard deviation serve as input to the second step of the inversion. That is, implicitly, a Gaussian distribution is assumed. Most likely, however, the posterior distribution associated with this first step is non-Gaussian, as such introducing the (unknown) errors. Secondly, as the subsequent step involves many independent 1-D inversions, it fails to honour the lateral correlation of the shear wave velocity in the subsurface. To improve the lateral correlation in the second step, Lehujeur *et al.* (2021) suggested inverting all the local dispersion

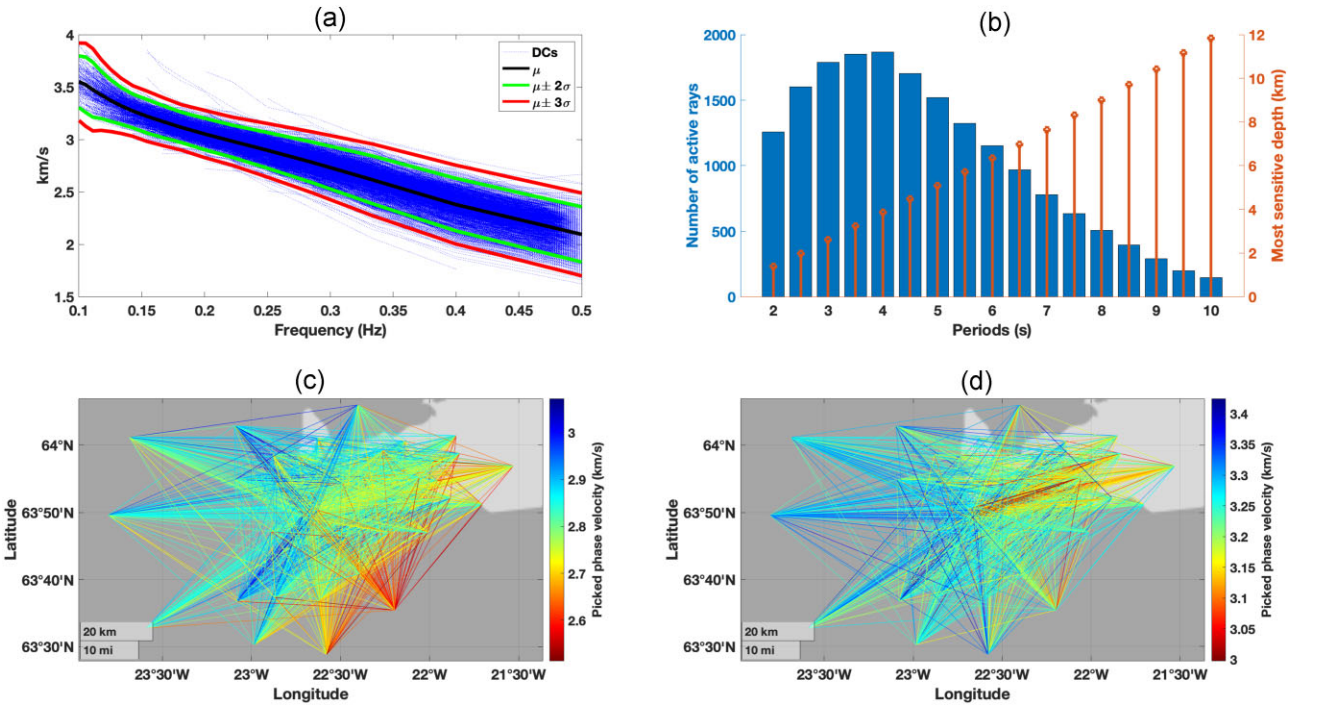

Figure 3. Analysis of picked dispersion curves. (a) All picked dispersion curves (blue) and their mean (μ; black curve). The green curves show $\mu \pm 2\sigma$ and the red curves show $\mu \pm 3\sigma$, where σ is the standard deviation. Data outside of the two red curves are discarded as outliers. (b) The number of active rays per period used in the inversion (blue bars), and the most sensitive depth related to each period (red stem plot). Active rays at periods of (c) 3.5 s and (d) 7 s are depicted as straight rays with the colour of each ray indicating the corresponding phase velocity.

curves simultaneously using a linearized 3-D inversion algorithm. In a similar vein, Fang *et al.* (2015) combined the two inversion problems into one. They proposed a one-step linearized 3-D inversion algorithm to recover the 3-D shear wave velocity directly from the frequency-dependent phase or group traveltimes. Recently, Zhang *et al.* (2018) proposed another one-step 3-D surface wave tomography algorithm using a reversible jump Markov chain Monte Carlo (rjMcMC), which we refer to as the one-step transdimensional method. It recovers the shear wave velocity directly from the frequency-dependent traveltimes.

$$\mathbf{d}(\mathbf{x}_k, \mathbf{x}_l, f_i) \xrightarrow{F^{-1}\left[\mathbf{d}(\mathbf{x}_k, \mathbf{x}_l, f_i)\right]} v_s(x, y, z), \tag{3}$$

where F^{-1} represents the one-step transdimensional probabilistic algorithm (i.e. the rjMcMC approach). Importantly, this one-step transdimensional algorithm results in an estimate of the posterior probability density. This implies that it allows us to quantify the uncertainty. In this case, we use the pointwise standard deviation of the ensemble of models for this purpose. This is the standard deviation with respect to the pointwise average of the same ensemble [i.e. at each position (x, y, z), standard deviation and average of the shear wave velocities are computed using all retained models]. The pointwise average has been shown to closely resemble the true velocity structure (Bodin & Sambridge 2009; Zhang *et al.* 2018; Rahimi Dalkhani *et al.* 2021). This one-step algorithm is illustrated in Fig. S2.

One-step transdimensional tomography involves the use of the reversible jump Markov chain Monte Carlo method which deploys a variable model geometry, a variable number of cells partitioning the model space and an unknown noise level in the input data. As such, the algorithm avoids the selection of fixed parametrizations and any regularization in the inversion process. This makes the algorithm less dependent on (often) subjective choices. Like many McMC algorithms, the one-step transdimensional algorithm starts with a random initial model, which is parametrized by Voronoi polyhedra with a randomly chosen number of Voronoi cells. The shear wave velocity is also assigned to each Voronoi cell randomly. The shape or geometry of each Voronoi cell is then defined by the surrounding cells. We refer to Zhang *et al.* (2018) and Rahimi Dalkhani *et al.* (2021) for a detailed description of the 3-D Voronoi partitioning.

The next step of the algorithm (which yields the second sample of the Markov chain) is to perturb the initial velocity model using one of the five possible perturbation steps, including a move step, a velocity update step, a birth step, a death step and a noise update step. After the perturbation, we compute the shear wave velocity on a fine rectangular grid so that the velocity can be used in the forward function to calculate the frequency-dependent traveltimes. For a detailed description of the workflow, we refer to Rahimi Dalkhani *et al.* (2021). These traveltimes are then compared with the measured surface wave phase traveltimes. The new velocity model is accepted or rejected based on the acceptance probability (see Bodin *et al.* 2009; Zhang *et al.* 2018, for more details). Continuously sampling the model space [i.e. proposing new $v_s(x, y, z)$], we asymptotically approach the posterior probability distribution of the model parameters. The pointwise average and standard deviation of these samples are subsequently computed, yielding the most probable velocity model and associated uncertainty, respectively. In order to remove the effects of the initial velocity model on the posterior distribution, an initial set of samples is discarded (usually referred to as the 'burn-in period'). In addition, to ensure the collected samples are uncorrelated, samples are retained at only a certain level (e.g. every 200 iterations); this process is usually referred to as 'thinning'.

5.2 Application to the extended IMAGE data

Prior to our probabilistic inversion, we recover an average 1-D shear wave velocity profile of the study area using a 1-D inversion algorithm (Xia *et al.* 1999). We used the mean phase velocities (the black curve in Fig. 3a) in this 1-D least-squares iterative algorithm. We used a 1-D velocity profile based on Tryggvason *et al.* (2002) as the initial model for this inversion. The recovered shear wave velocity profile is depicted in the Fig. S3(a). The sensitivity kernels at different periods are also depicted in the Figs S3(b) and (c). It shows that the sensitivity decreases significantly below 15 km depth. The recovered velocity is constant below 15 km depth, which is the most likely depth of the Moho discontinuity (e.g. Weir *et al.* 2001; Jacoby *et al.* 2007). To include this discontinuity, we sampled the subsurface down to 20 km depth (i.e. we populated it with Voronoi cells down to this depth). The half space below 20 km depth is assigned the velocity of the bottom layer (i.e. the velocity of the deepest Voronoi at each gridpoint), meaning that it is also laterally variable. Based on several studies focusing on the study area (e.g. Weir *et al.* 2001; Du *et al.* 2002; Foulger *et al.* 2003), the upper crustal shear wave velocity can reach 3.7 $\mathrm{km\,s^{-1}}$ and the lower crustal shear wave velocity can reach 4.2 $\mathrm{km\,s^{-1}}$. Consequently, we considered a uniform prior ranging from 1.5 to 4.5 $\mathrm{km\,s^{-1}}$ for the shear wave velocity. The upper bound of 4.5 $\mathrm{km\,s^{-1}}$ was chosen based on the fact that the shear wave velocity in the mantle has been shown to not exceed 4.5 $\mathrm{km\,s^{-1}}$ below the RP (e.g. Du *et al.* 2002; Foulger *et al.* 2003).

Table 1 lists the modelling and inversion parameters used in the application of the one-step transdimensional inversion to the surface wave data retrieved from the RP ambient noise data. An arbitrary first model (the 'initial model') was chosen, meaning that the number of Voronoi cells, their positions, and their velocities were chosen randomly. We used a coarser grid to compute the frequency-dependent traveltimes (forward modelling) while sampling the model space, and a finer grid for calculating the post-burn-in pointwise average and standard deviation of the sampled models.

Gaussian proposal (probability) distributions are used for drawing new velocity values and new nuclei. The proposal width of these Gaussian distributions affects the chance of a proposed model being accepted and consequently the transdimensional algorithm's convergence rate. Too narrow or too wide proposal distributions both result in slower convergence rates. A narrow proposal distribution increases the acceptance ratio but explores the parameter space more locally. By contrast, a wide proposal distribution explores the space more widely but leads to lower acceptance ratios and as such also to a slower convergence rate (Rahimi Dalkhani *et al.* 2021). According to previous research, an effective proposal width results in a 25–50 per cent acceptance rate (Bodin *et al.* 2009; Gelman *et al.* 1996). The width of the proposal distributions listed in Table 1 are determined in a previous, purely synthetic study, but using the same station configuration (Rahimi Dalkhani *et al.* 2021). This also applies to the proposal widths of the noise hyperparameters (detailed in the paragraph below).

We assumed a (non-informative) uniform prior probability distribution for the model parameters. What we refer to as the 'valid range' in Table 1 defines, for each parameter, the range for which the prior probability is non-zero. To reduce computational costs, while still preserving the non-linearity of the problem we updated ray paths every 250 iterations (similar to Rahimi Dalkhani *et al.* 2021). Thinning was achieved by retaining every 200th model. The noise was assumed to be uncorrelated and normally distributed, with the variance being a frequency-dependent, linear function of traveltime, that is with d_i representing the ith element of the data vector $\mathbf{d}$ (and hence traveltime), $\sigma_i = a{*}d_i + b$. This linear relationship between traveltime and traveltime error is usually assumed (e.g. Bodin *et al.* 2012; Galetti *et al.* 2017; Zhang *et al.* 2020; Rahimi Dalkhani *et al.* 2021). The a and b are assumed to be unknown and therefore also estimated by the Markov chain process (see, e.g. Bodin *et al.* 2012).

To sufficiently sample the posterior distribution, we used 20 independent McMC chains, each sampling 3×10^6 samples from the posterior probability density of model parameters given the frequency-dependent traveltimes. Fig. 4 shows some statistical measures of these 20 McMC chains. Different colours represent different sampling chains. Noise hyper-parameters are presented for a single frequency as they vary by frequency. We observe that the misfit, the number of cells, and the noise hyper-parameters stabilize after generating approximately 0.5×10^6 samples. This suggests that the Markov chain has mixed sufficiently well and that the posterior probability density is properly sampled. To be on the safe side, however, we discarded the first million samples (usually referred to as the burn-in phase). The rest of the samples are retained at every 200th iteration. Consequently, combined the 20 chains lead to a total of 200 000 posterior samples to be retained. These are subsequently used to compute pointwise mean and variance. Residual phase velocity errors are provided in Fig. S4.

6 TOMOGRAPHIC RESULTS

We present the pointwise average of the retained post-burn-in samples as our final tomographic solution and the pointwise standard deviation of retained samples as the uncertainty related to the solution model. Several horizontal and vertical slices of the posterior mean are presented in Figs 5–9. Only the most densely sampled region of the study area is presented, which has lower uncertainties; an area of approximately 38 km by 45 km (see the dashed black box in Figs 1 or B1). The model uncertainties are presented in Appendix B. The uncertainty for the whole area covered by the seismic stations (120 km by 70 km) is presented in Fig. B1. Figs B2–B5 are the posterior standard deviation (i.e. uncertainty) associated with the posterior mean presented in Figs 6–9, respectively. As expected, the areas with more seismic stations show lower uncertainty due to the higher number of station–station paths in these areas. We have selected the most reliable area based on these uncertainties.

Fig. 5 shows the pointwise mean of the shear wave velocity beneath the RP at six different depths (0.5, 3, 4, 6, 8 and 10 km). The coastline and the three known HT fields of Reykjanes, Eldvörp-Svartsengi and Krýsuvík (black dashed polygons in Fig. 1) are included in these figures for reference. It should be noted that the HT polygons show the extent of the geothermal fields, according to the resistivity values (the resistive core) at 1 km depth (as summarized in Flóvenz *et al.* 2022). Significant velocity anomalies are observable in Fig. 5. At shallow depths (0.5 km; Fig. 5a) the Eldvörp-Svartsengi and Krýsuvík HT geothermal fields show high-velocity anomalies, the same applies to the Fagradalsfjall volcanic system. The anomalies invert at depths of around 2 km. At a depth of 3–6 km (Figs 5b–d) the known HT fields appear as low-velocity anomalies, most pronounced at Eldvörp-Svartsengi, Krýsuvík and in the vicinity of the Fagradalsfjall's recent eruption site (yellow star in Fig. 5). The low-velocity at Reykjanes is most pronounced from 6 to 8 km depth (Figs 5d and e). A striking NW–SE trending low-velocity anomaly, almost perpendicular to the Krýsuvík volcanic system, is apparent in Figs 5(c)–(f). At the depth of 4 km (Fig. 5c)

Table 1. Modelling and sampling parameters used in the probabilistic one-step inversion of the interferometric traveltimes.

Modelling and sampling parameters	Value
Model dimension (km)	120 (east–west)× 70 (north–south) × 20
Number of gridpoints in McMC sampling	121 × 71 × 41
Number of gridpoints for calculating post-burn-in pointwise average	241 × 141 × 81
Valid range of shear wave velocity (km s^{-1})	1.5–4.5
Valid range of noise hyperparameter *a*	10^{-5}–1
The valid range of noise hyperparameter *b*	0–2
Proposal width for a move step. *Md* is the model dimension	0.07∗*Md*
Velocity proposal width (km s^{-1})	0.3
Proposal width for *a*	10^{-3}
Proposal width for *b*	10^{-2}
Thinning level	200
Ray path update step	250
Number of sampling chains	20
Number of samples per chain	3 × 10^6
Number of burn-in samples per chain	1 × 10^6

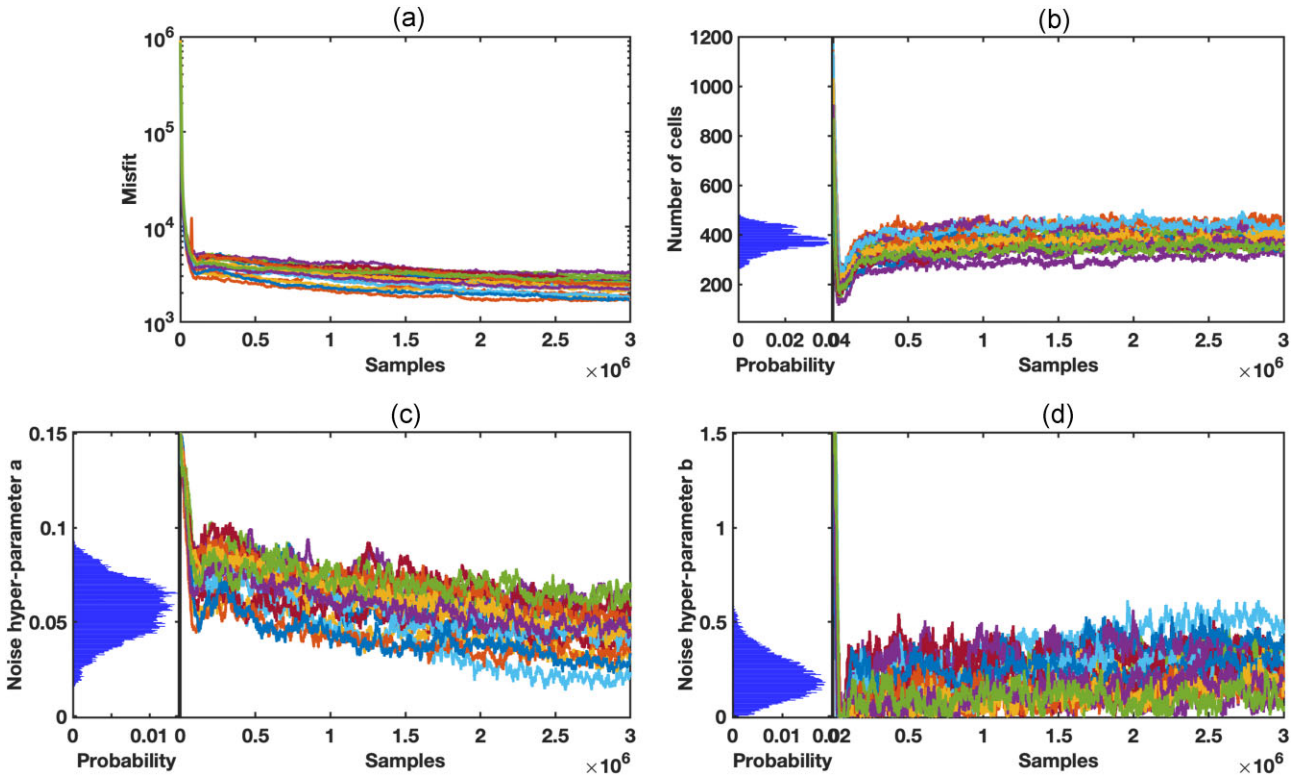

Figure 4. Chain statistics of the 20 McMC chains. Each colour represents a different chain. (a) Misfit, (b) number of cells, (c) the noise hyperparameter *a* and (d) the noise hyper-parameter *b*. Histograms of the posterior distribution for the retained models for each parameter are shown as insets on the left side of each panel in (b–d). These graphs are used to assess the convergence of the sampler.

the low-velocity anomalies are small and mainly limited to the HT fields of Eldvörp-Svartsengi and Krýsuvík. At 8 km depth (Fig. 5e), however, the area is dominated by low shear wave velocities, where the NW–SE Krýsuvík anomaly is the strongest. A weak trend along the plate boundary (N70°E) is observable in both the high-velocity of Fig. 5(a) and low-velocity of Fig. 5(b).

Differences are observed in the shape and size of the low-velocity patches with respect to the known HT fields constrained by resistivity data at 1 km depth (black dashed lines in Fig. 5; Flóvenz *et al.* 2022). At depths of 6–8 km below the Reykjanes HT field (Figs 5d and e), the low-velocity anomaly is smaller than the HT field and placed slightly north of it. Within the Eldvörp-Svartsengi HT field, the low-velocity anomaly is located right below the corresponding HT field at a depth of 4 km (Fig. 5c) with a comparable size. However, the size of the low-velocity anomaly is greater than the corresponding HT field at the depth of 6 km and stretching to the north. The Krýsuvík low-velocity anomaly is the most prominent, that is both the largest and the strongest anomaly we observe on the RP, while it is slightly smaller in size than the corresponding HT field. At 4–10 km depth it stretches from the centre of the HT field towards the southeast, almost perpendicular to the volcanic system (Figs 5c–e).

In the vicinity of the Fagradalsfjall 2021–2023 eruption sites (yellow star in Fig. 5), we observe low-velocity anomalies at 4–6 km

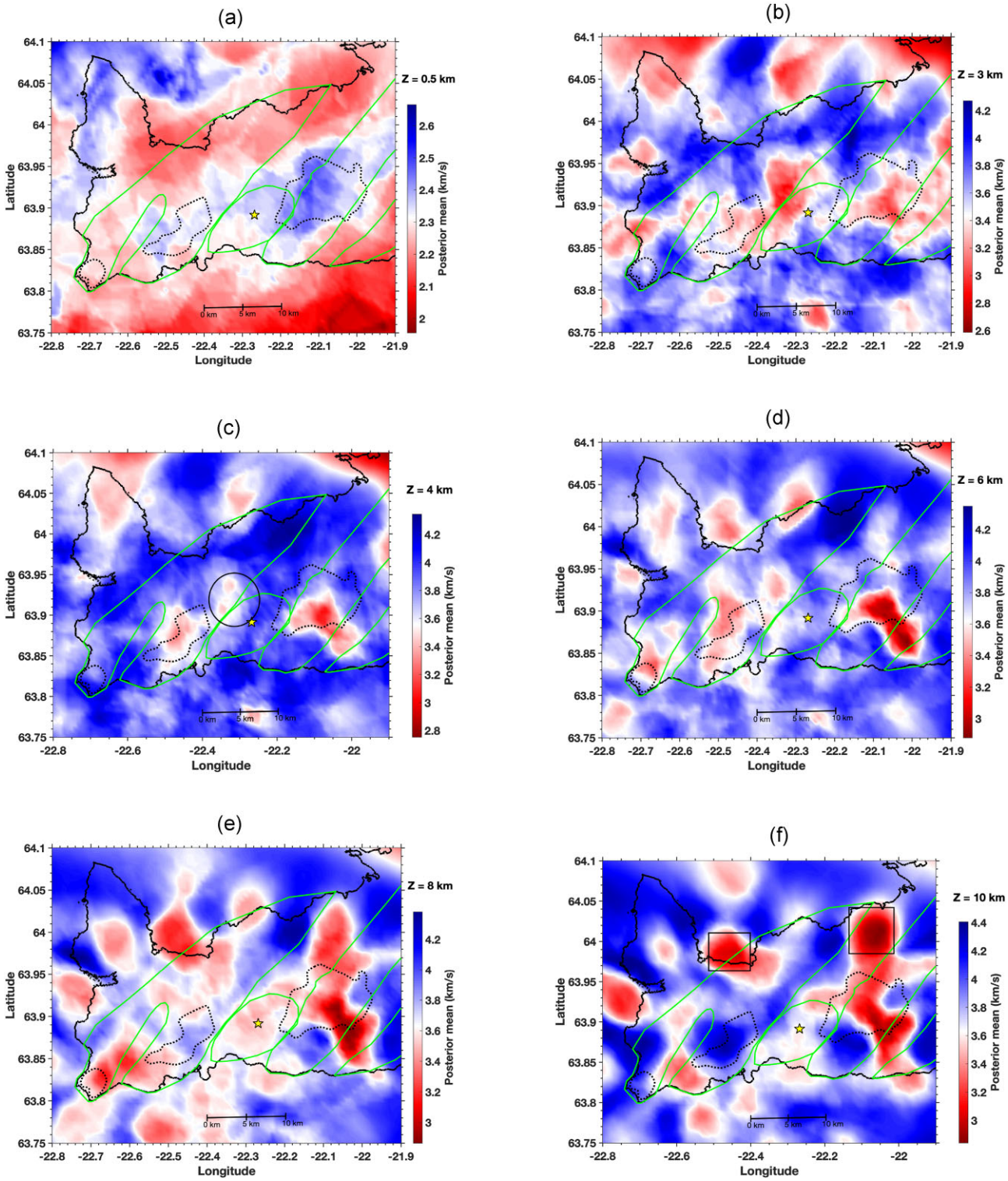

Figure 5. Pointwise averaged shear wave velocities (from the retained post-burn-in samples) at six different depths: (a) 0.5 km, (b) 3 km, (c) 4 km, (d) 6 km, (e) 8 km and (f) 10 km, of the area with the highest resolution and the lowest uncertainties (38 km by 45 km). The green polygons show the outlines of the volcanic systems. The dashed black polygons are the known high-temperature geothermal fields. The black circle in (c) indicates the low-velocity observed at the boundaries of the Eldvörp-Svartsengi and Fagradalsfjall volcanic systems. The yellow star inside the Fagradalsfjall volcanic system is the approximate location of the 2021, 2022 and 2023 eruptions. Note that the colour scale is not the same on all slices. Uncertainties (posterior standard deviation associated with the posterior mean presented) are displayed in Fig. B1.

depth at the boundaries of the Eldvörp-Svartsengi and Fagradalsfjall volcanic systems. The Fagradalsfjall anomalies, however, are all fairly weak. Finally, two significant low-velocity anomalies are observed at 10 km depth (Fig. 5f) indicated by black rectangles. Due to the low density of ray paths at these two locations (see Figs 3c–d) we refrain from interpreting these anomalies. Furthermore, the uncertainties of both anomalies are very high in Figs B1(e), (f) and B3(d).

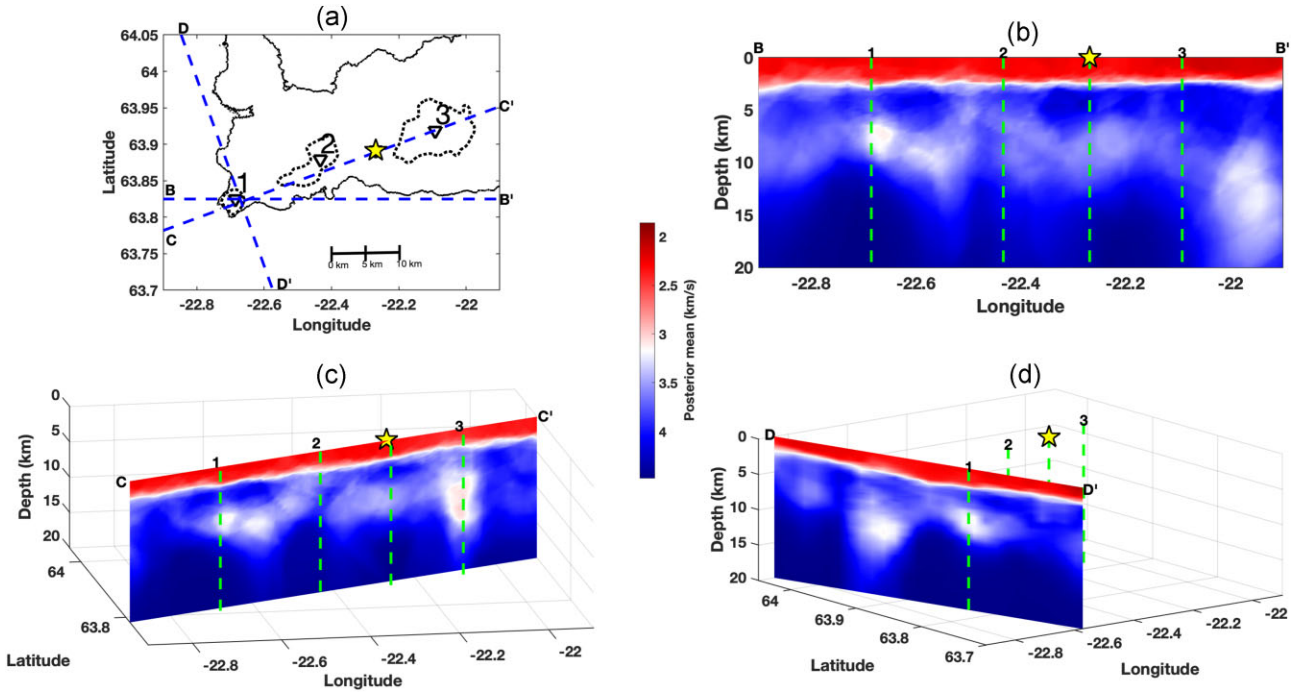

Figure 6. Vertical cross-sections, centred at the location of the Reykjanes HT geothermal field, of the pointwise averaged shear wave velocities of the retained post-burn-in samples. (a) Map of the area showing the location of the three reference points, and the extent of the known high-temperature geothermal fields of Reykjanes, Svartsengi and Krýsuvík (dashed black polygons), blue lines show the locations of the vertical cross-sections of the shear wave velocities along an east-west profile (b), N70°E oriented profile (c) and N20°W oriented profile (d). The yellow star is the approximate location of the 2021, 2022 and 2023 eruptions. Uncertainties (posterior standard deviation associated with the posterior mean presented) are displayed in Fig. B2.

To better visualize the velocity structure of the RP focusing on the HT geothermal fields, we present the recovered 3-D velocity structure in three differently oriented vertical cross-sections centring at the Reykjanes, Eldvörp-Svartsengi and Krýsuvík HT fields, and the Fagradalsfjall eruption site, respectively (Figs 6–9). In each figure, the first vertical cross-section is oriented along an east–west profile (B–B'), the second along a profile striking N70°E (C–C'), approximately along the plate boundary, and the third cross-section is along a profile striking N20°W (D–D'), approximately perpendicular to the plate boundary. We observe, in general, across the whole survey area, that the shear wave velocity increases with depth from about 2 km s^{-1} at the surface to approximately 3.8 km s^{-1} at a depth of 5 km. A decrease in shear wave velocity with depth (due to a large number of low-velocity anomalies) is generally observed across the RP between depths of 4–8 km, but notably shallowest under the HT fields.

Figs 6(b)–(d) present the vertical cross-sections centred at the location of the Reykjanes power plant and hence centred at the Reykjanes HT geothermal field (labelled '1' in map view and on the cross-sections), The B–B' cross-section (Fig. 6b) lies across the Reykjanes HT field and along the coast to the east. A low-velocity patch is observed directly below the Reykjanes HT field. Between 6 and 8 km depths, it extends laterally towards the east, passing the area below the Eldvörp-Svartsengi HT field, the Fagradalsfjall volcanic system, and all the way east of the Krýsuvík HT field. The C–C' cross-section in Fig. 6(c) transects all four volcanic systems of Reykjanes, Eldvörp-Svartsengi, Fagradalsfjall and Krýsuvík along the plate boundary. It shows a similar low-velocity image as Fig. 6(b), but here the Reykjanes anomaly is clearer, and also the connection to Eldvörp-Svartsengi to the NE. A large low-velocity zone is visible below the Krýsuvík HT field (labelled '3'). Slightly lower velocities are also observed at 7–10 km depth at a longitude of −22.3°W, located between '2' and '3', where the Fagradalsfjall volcanic system lies. This anomaly seems weakly connected to the Krýsuvík low-velocity anomaly (Fig. 6c). The low-velocities seem to highlight a more or less continuous zone along the plate boundary at *ca*. 6–10 km depth. The low-velocity patch below the Reykjanes HT field is also observable in Fig. 6(d), cross-section D–D', down to 8 km depth. Another significant low-velocity anomaly at 6–10 km depth can be seen to the north–northwest of the Reykjanes HT field in Fig. 6(b).

Fig. 7 presents the vertical cross-sections centred at the location of the Svartsengi power plant, labelled '2'. A low-velocity anomaly is observable below the Eldvörp-Svartsengi HT field on cross-section B–B'. This low-velocity zone appears at around 3 km depth and extends to approximately 7 km depth, dipping from E to W with an approximate lateral extent of 8–10 km (Fig. 7b). This low-velocity patch is visible in Fig. 7(c) as well. A horizontal low-velocity anomaly at around 6 km depth in Fig. 7(c) is observed possibly linking the Reykjanes and Eldvörp-Svartsengi HT fields at depth. Below the Krýsuvík HT field, the pronounced low-velocity column (see Fig. 6c) is again visible in Figs 7(b) and (c). Below the Fagradalsfjall volcanic system, the low-velocity patch observed at around 8 km depth in Fig. 6(c) is also visible in Figs 7(b) and (c).

Fig. 8 presents the vertical cross-sections centred at the Krýsuvík HT field (labelled '3'). A large and prominent low-velocity column is clearly observable below the Krýsuvík HT field at roughly 5–12 km depth in all three vertical cross-sections. Fig. 8(d) also shows clearly that the pronounced low-velocity anomaly is extending to the southeast and it is the shallowest of all three, reaching up to about 3 km depth, just southeast of '3'. Due to the 2021–2023

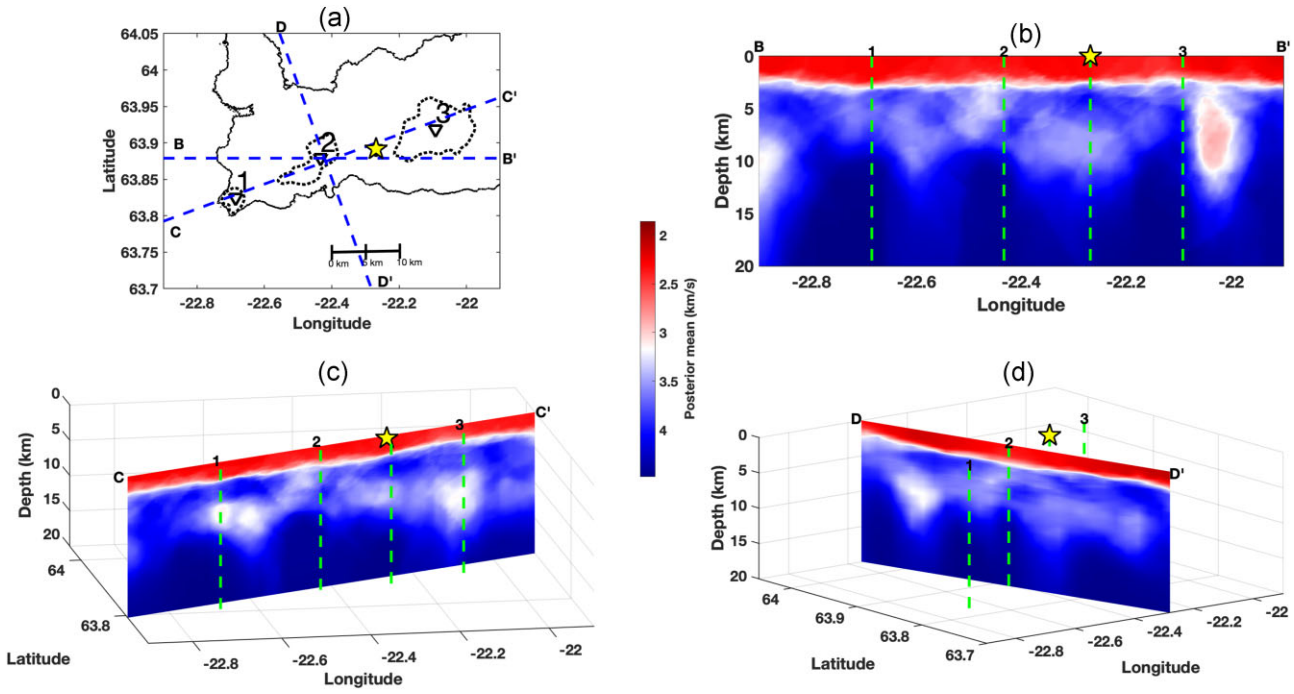

Figure 7. Vertical cross-sections, centred at the location of the Eldvörp-Svartsengi HT geothermal field, of the pointwise averaged shear wave velocities of the retained post-burn-in samples. (a) Map of the area showing the location of the three reference points, the transects associated with the vertical cross-sections (blue dashed lines), and the extent of the known high-temperature geothermal fields of Reykjanes, Eldvörp-Svartsengi and Krýsuvík (black dashed polygons). Cross-sections of the shear wave velocities along an east–west profile (b), N70°E oriented profile (c) and N20°W oriented profile (d) are shown. The yellow star is the approximate location of the 2021, 2022 and 2023 eruptions. The vertical green dashed lines on the cross-sections indicate the extension of the corresponding point in depth for reference. Uncertainties are displayed in Fig. B3.

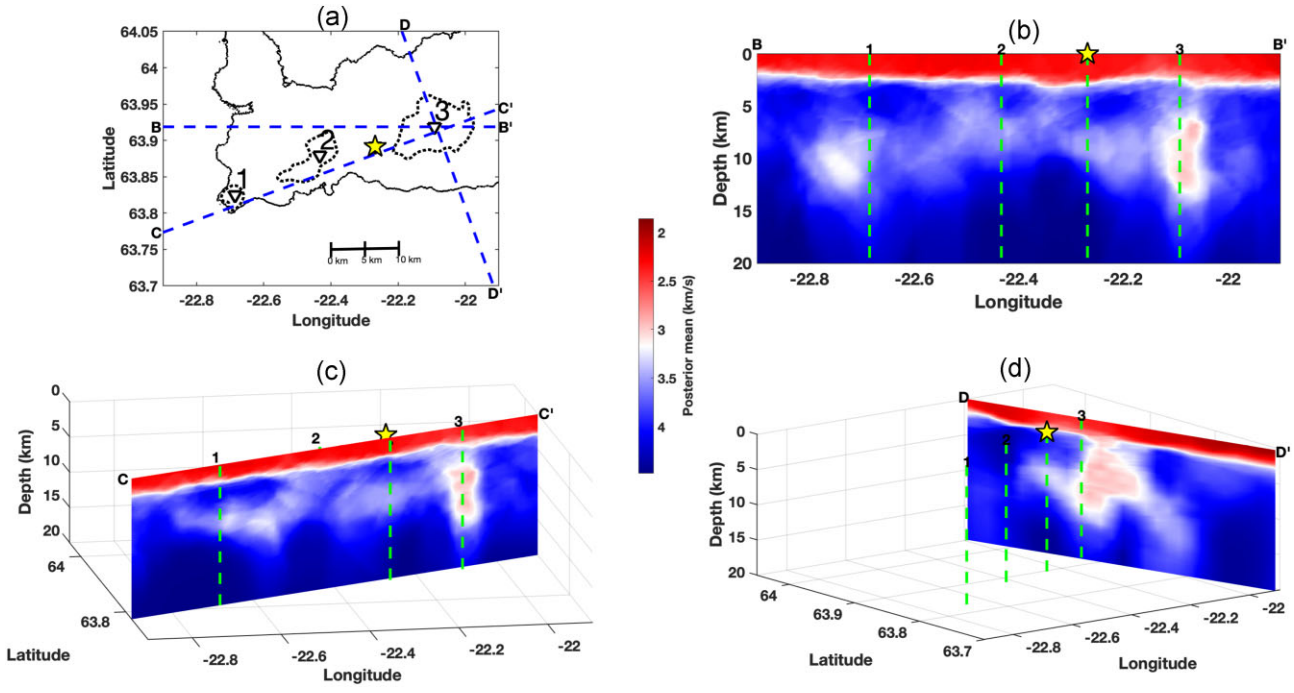

Figure 8. Vertical cross-sections, centred at the location of the Krýsuvík HT geothermal field, of the pointwise averaged shear wave velocities of the retained post-burn-in samples. (a) Map of the area showing the location of the three reference points, the transects associated with the vertical cross-sections (blue dashed lines) and the extent of the known high-temperature fields (black dashed polygons). Cross-sections of the shear wave velocities along an east–west profile (b), N70°E oriented profile (c) and N20°W oriented profile (d) are shown. The yellow star is the approximate location of the 2021, 2022 and 2023 eruptions. Uncertainties are displayed in Fig. B4.

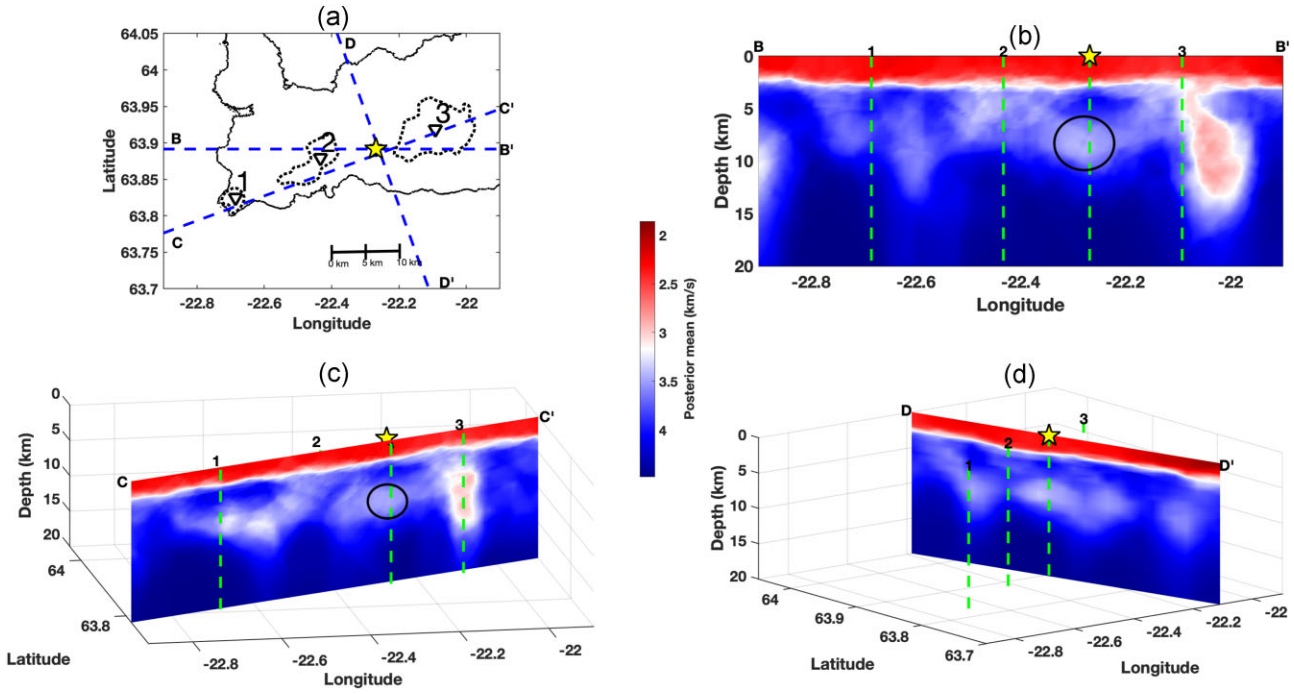

Figure 9. Vertical cross-sections, of the pointwise averaged shear wave velocities, centred at the location of the 2021–2023 eruptions site, within the Fagradalsfjall volcanic system. (a) Map of the area showing the location of the three reference points, the transects associated with the vertical cross-sections (blue dashed lines), and the extent of the known high-temperature fields (black dashed polygons). Cross-sections of the shear wave velocities along an east–west profile (b), N70°E oriented profile (c) and N20°W oriented profile (d) are shown. The yellow star is the approximate location of the 2021, 2022 and 2023 eruptions. The black circles in (b–c) indicate the low-velocity observed below the Fagradalsfjall volcanic system. Uncertainties are displayed in Fig. B5.

volcano-tectonic unrest on the RP, we also present the vertical cross-sections centred at the location of the recent eruption site in Fig. 9. It should however be noted that the data used in this study are from 2014 to 2015.

To summarise the most important observations, which will be discussed in the next section:

(i) In general, from the top (Earth's surface) to the bottom (20 km) of the model, the pointwise average of the sampled shear wave velocity increases, but a decrease in velocity is observed within the depth range of 5–8 km.

(ii) Close to the surface within and around the known HT geothermal fields, and somewhat NE–SW along the fissure swarms of the RP, relatively high-velocity patches are observed (Fig. 5a). At depths greater than 3 km, these higher velocities invert (decrease) to relatively low-velocities (in comparison to shear wave velocities in the same horizontal plane).

(iii) Low-velocities are dominant at depths of 6–8 km, but beneath the HT fields, the low-velocities rise up to 3–4 km depth.

(iv) The size and location of these low-velocity bodies coincide overall fairly well with the extent of the HT geothermal fields derived from electrical resistivity studies, despite deviating somewhat.

(v) A large and strong low-velocity anomaly is observed below the Krýsuvík HT geothermal field, and extends down to around 15 km depth. This pronounced anomaly stretches from the centre of the HT field towards the southeast from a depth of 3 km.

(vi) A low-velocity zone is observed at the northwest border of the Fagradalsfjall volcanic system, at a depth of approximately 4–5 km (Figs 5c and d). This low-velocity slopes down to below the recent eruption site at a depth of 7–9 km (Figs 9b–d).

(vii) The shear wave velocity below 15 km depth is almost constant with velocities above 4.2 km s^{-1}.

7 DISCUSSION

In this section, we provide an interpretation of the pointwise averaged shear wave velocities, qualitatively comparing our final model to other geophysical models, and relating it to the existing geological and geophysical literature and interpretation of the RP. Prior to interpreting the observed shear wave velocities, we consider our models' resolution. Resolution tests using synthetic surface wave responses for the RP and the extended IMAGE seismic network station configuration are presented in a previous study (Rahimi Dalkhani *et al.* 2021). In that study, we concluded that for the area of interest (black box in Fig. 1), the transdimensional algorithm is able to recover quite well a 3-D velocity model with blocks of 5 by 5 by 2.5 km (in the north, east and depth directions, respectively). This suggests that structures of that size (or larger) are well resolved.

7.1 High-velocity anomalies

The first observation is the relatively high shear wave velocities close to the surface around the location of the known HT geothermal fields (compared to the surrounding areas; Fig. 5a). This is in particular valid for Eldvörp-Svartsengi and Krýsuvík, where the anomalies also show a weak trend along the fissure swarms; whereas the anomaly in Reykjanes is very small. It is worth noting that the Reykjanes HT field is much smaller in areal extent than the Eldvörp-Svartsengi and Krýsuvík HT fields based on the resistivity studies. Our findings are consistent with a high-velocity zone found by Adelinet *et al.* (2011) around the Krýsuvík HT field at a depth of 2 km. Similarly, Jousset *et al.* (2016) observed high shear wave velocities for the Reykjanes and Eldvörp-Svartsengi HT fields at a depth of 200 m. An explanation for the relatively high-velocity

zones near the surface at the location of the HT geothermal fields could be the intense mineral alteration (caused by higher temperatures) in the uppermost 1–2 km, filling up pores and fractures which in turn increases the seismic velocities in those areas near the surface.

7.2 Brittle–ductile transition

The second notable observation is the horizontally extended velocity decrease between 5 and 8 km depth dominating the whole area (Figs 6–9b and c), in comparison to higher velocities at greater depth. This low-velocity anomaly domes up to a depth of 3 km below all the known HT fields. This kind of low shear wave velocity anomaly is commonly observed within volcanic systems (Takei 2017), and commonly attributed to partial melt (e.g. Lees 2007). However, some geochemical observations (e.g. McKenzie 2000) suggest that the melt fraction is too small in an area with partial melt (0.1 per cent) to have the shear wave velocity drop significantly (Priestley & McKenzie 2006; Takei 2017). Additionally, the temperature at the location of low-velocity anomalies within the volcanic systems is sometimes lower than the solidus temperature of the rocks. For example, the solidus temperature of basalt (i.e. the main composition of rocks in RP's crust) exceeds 1000 °C (Chen *et al.* 2017), whereas the temperature is estimated to be around 600 °C at a depth of 6–7 km on the RP (Violay *et al.* 2012; Bali *et al.* 2020), representing the BDT zone, evidenced by the IDDP-2 drilling.

Recent studies suggest that these low shear wave velocity anomalies are more likely due to the combination of high temperature and an-elasticity (Priestley & McKenzie 2006, 2013; Karato 2014; Takei 2017). An-elasticity makes the effect of increasing temperature significant by decreasing the shear wave velocity rather abruptly (Takei 2017). In our case, the an-elasticity is likely associated with the known BDT zone, between the upper crust and the lower crust, which is estimated to be at around 6–7 km depth on the RP, doming up to 3–5 km depth below the HT geothermal fields (Blanck *et al.* 2020; Gudnason *et al.* 2020; Flóvenz *et al.* 2022). The BDT depth range coincides well with our observation of a general velocity decrease within the depth range of 5–8 km, suggesting that an-elasticity and elevated temperatures also play a significant role in the shallow onset of the velocity-decrease at around 3 km depth below the HT fields.

7.3 Magma accumulation

Recently, Caracciolo *et al.* (2023) presented an interesting conceptual model for the magma plumbing architecture on the RP, based on petrochemical analysis of the lava flows of the 800–1240 AD Fires on the Peninsula. This was the last volcano-tectonic episode prior to the 2021–2023 Fagradalsfjall episode, with eruptions within all the volcanic systems of the RP, except Fagradalsfjall. Caracciolo *et al.* (2023) find that during the 800–1240 AD Fires, magma accumulation occurred at around 7–10 km depth below the Reykjanes, Eldvörp-Svartsengi and Krýsuvík systems, a controlling factor for volcanic eruptions within these systems. However, deeper plumbing structure applies to the Fagradalsfjall system, where petrochemical analysis of the 2021 magma shows that it was tapped directly from near-Moho reservoirs at 15–20 km depth, with little or no stalling in the uppermost crust prior to eruptions (Halldórsson *et al.* 2022).

The depth extent of where the low-velocity anomalies are intensified in our model, at a depth of 7–10 km between the Reykjanes and Eldvörp-Svartsengi HT fields and at a depth of 5–12 km depth below the Krýsuvík HT field (vertical cross sections along the plate boundary in Figs 6–8c), is in good agreement with the magma plumping architecture suggested by Caracciolo *et al.* (2023).

7.4 HT geothermal fields

7.4.1 Krýsuvík volcanic system

The largest and most significant seismic feature we observe is related to the Krýsuvík volcanic system. Krýsuvík hosts an unharvested HT geothermal system, which heat source is considered to be dyke intrusions (Arnórsson *et al.* 1976; Arnórsson 1987; Hersir *et al.* 2020a), perhaps also indicated by an indicative gravity high in the area (Guðmundsson *et al.* 2004). The relatively wide vertical low-velocity column we observe seems to be centred 4 km west of Lake Kleifarvatn (Fig. 1). This coincides well with the results of a recent electrical resistivity study in the area, which indicated a large conductive body at approximately 2 km depth in the same area (Hersir *et al.* 2020a). The centre of this conductive body is labelled '3' in Figs 6–8, where it is also evident that the Krýsuvík HT field is the largest out of the three known HT fields, as determined by both resistivity studies and ANSWT.

The conductive body of Hersir *et al.* (2020a) is located near the central part of the Krýsuvík geothermal area, where its body concurs horizontally with the source of inflation and deflation observed in Krýsuvík since 2009 with both GPS and InSAR measurements, modelled at 4–5 km depth (Michalczewska *et al.* 2012; Flóvenz *et al.* 2022). Adelinet *et al.* (2011) suggest the presence of a gaseous or supercritical fluid at around 6 km depth, based on the analysis of *P*- and *S*-wave tomographic results. Hobé *et al.* (2021) also predict a large supercritical reservoir below 5 km depth.

The pronounced low-velocity anomaly extends from the Krýsuvík HT area to the southeast almost perpendicular to the Krýsuvík fissure swarm. Anomalies perpendicular to the main geological structures are not uncommon within HT fields in Iceland. This is observed in Reykjanes (e.g. Khodayar *et al.* 2018), Krafla (e.g. Árnason 2020) and in Hengill (e.g. Hersir *et al.* 1990; Árnason *et al.* 2010; Obermann *et al.* 2022). In Hengill, a resistivity low, a zone of intense geothermal surface manifestations, and a magnetic low, all transect the Hengill volcanic system. In Krýsuvík, our observed low-velocity anomaly coincides fairly well with a vague zone of geothermal surface manifestations as well as trends of low resistivity structure caused by hydrothermal alteration (Hersir *et al.* 2020a).

7.4.2 Fagradalsfjall volcanic system

The Fagradalsfjall volcanic system is of enhanced interest due to the 2021–2023 volcano-tectonic rifting event (e.g. Fischer *et al.* 2022; Halldórsson *et al.* 2022; Pedersen *et al.* 2022; Sigmundsson *et al.* 2022). The Fagradalsfjall volcanic system differs in both size and in terms of eruption frequency compared to other volcanic systems on the RP (Sæmundsson *et al.* 2020). Most of the volcanic systems have experienced volcanism and rifting events every 800–1000 yr for the last 4000 yr, while Fagradalsfjall has not experienced

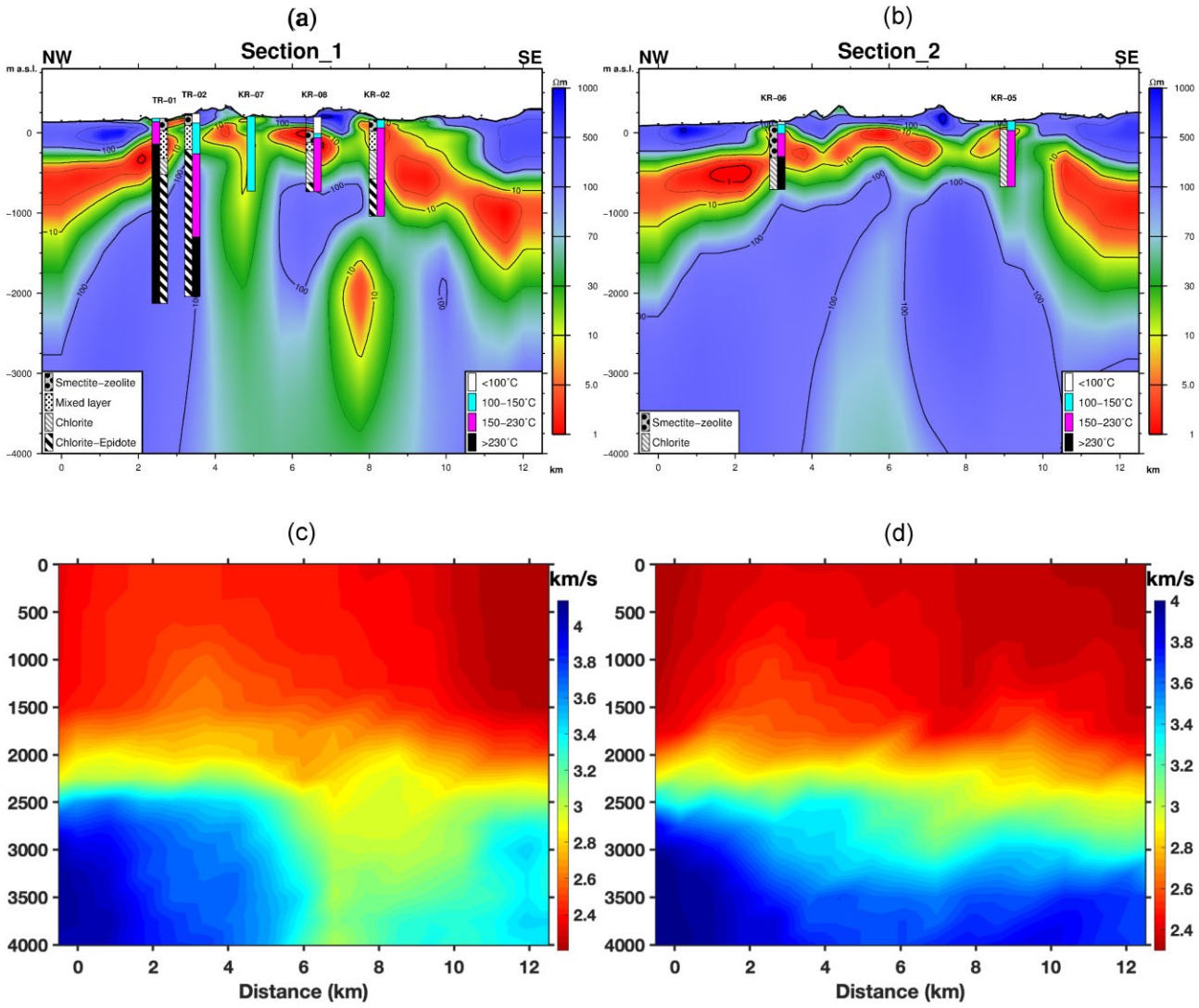

Figure 10. Vertical cross-sections transecting the Krýsuvík volcanic system; comparing the electrical resistivity (a, b) and the recovered shear wave velocity (c, d). The two electrical resistivity profiles (a, b) show hydrothermal alteration and measured temperature in wells close to the cross-sections (taken from Hersir *et al.* 2020a with permission from Elsevier [License number: 5673120502348]). The location of the two cross-sections is depicted in the Fig. S5.

volcanism for over 6000 yr (Sæmundsson *et al.* 2020). According to the literature (e.g. Flóvenz *et al.* 2022), there is no known HT geothermal field within the Fagradalsfjall volcanic system (Fig. 1), but notably, no resistivity survey has been carried out nor have exploratory wells been drilled in the area. At this point in time, there is not much published on the geophysics of the Fagradalsfjall volcanic system.

We observe a low-velocity anomaly at the depth of 4 km at the boundaries of the Eldvörp-Svartsengi and Fagradalsfjall volcanic systems, indicated by a black circle in Fig. 5(c). The anomaly extends to greater depths and towards the northwest in Fig. 5(d) with a perpendicular direction to the plate boundary. At the depth of 4 km (Fig. 5c), this low-velocity anomaly is located around 1 km northwest of the 2021, 2022 and 2023 Fagradalsfjall eruption sites indicated by the yellow star (Pedersen *et al.* 2022). Consequently, it is plausible that this low-velocity anomaly might be related to the recent eruptions in the area, perhaps aided by the suggested crustal weakening under tension at this location (Fischer *et al.* 2022). It should, however, be noted that the seismic data used in our ANSWT are from 2014 to 2015.

The vertical cross sections at the location of the recent eruptions sites (Fig. 9), display a rather high-velocity patch between 3 and 6 km depth, while the velocity decreases between 7 and 11 km depth. The seismicity within the brittle part of the RP crust between 2017 and 2022, is mostly confined to 2–6 km depth (Fischer *et al.* 2022; Ágústsdóttir *et al.* 2023) and, therefore, lies within the same depth range as the high shear wave velocity patch below Fagradalsfjall. The deep long-period earthquakes below Fagradalsfjall at 8–12 km depth observed by Greenfield *et al.* (2022) lie within the ductile part of the crust and are likely due to higher strain rates (fluid or gas movements). These deep earthquakes coincide with the low shear wave anomaly we observe between longitudes −22.3°W to −22.2°W at a depth of 7–11 km indicated by the black circles in Figs 9(b) and (c).

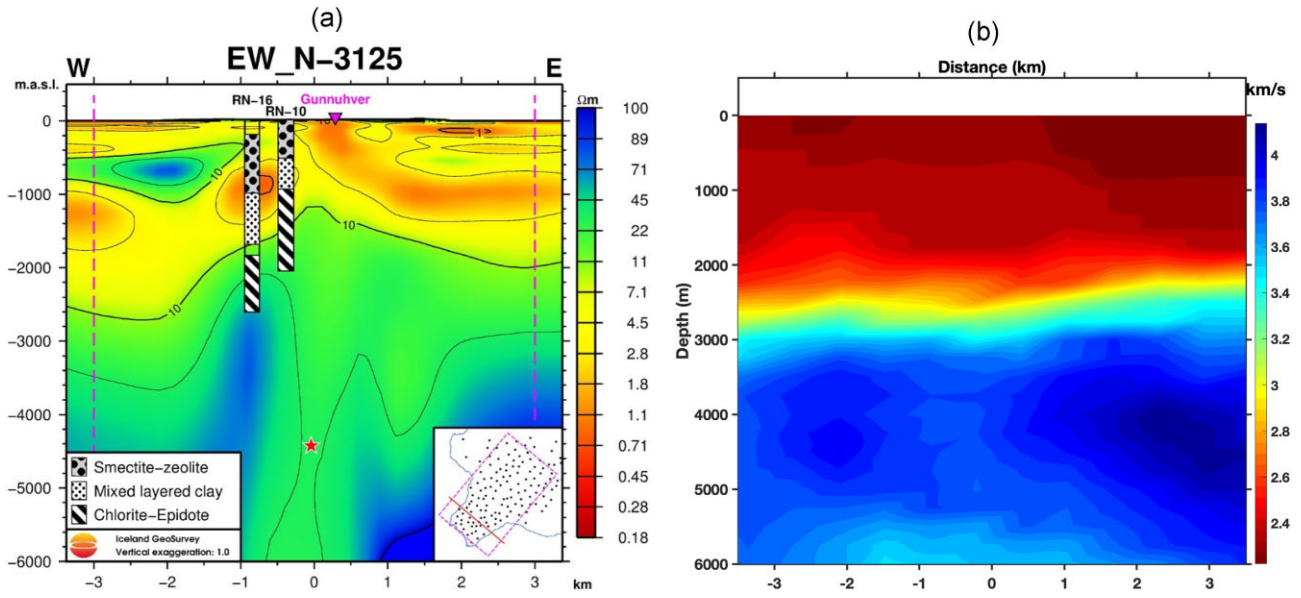

Figure 11. Cross-section transecting the Reykjanes volcanic system; comparing the electrical resistivity (a) and the recovered shear wave velocity (b). The electrical resistivity profile (a) shows hydrotherrmal alteration in wells close to the cross-section, the inset figure shows the location of the cross-section (taken from Karlsdóttir *et al.* 2020 with permission from Elsevier [License number: 5673120690717]). The red star marks the bottom of the IDDP-2 well.

7.4.3 Are there links between the HT fields on the RP?

In a number of our figures, there are hints of potential links between the HT fields on the RP (Figs 5–8). However, these could also reflect variations of the BDT zone, and the way cross-sections are plotted. In some cases, we are likely imaging the BDT zone and how it coincides in a location with the low shear wave anomalies below the HT fields, as in Fig. 6(b), but in other cases, we are likely imaging potential links, for examplw between Krýsuvík and Fagradalsfjall in Figs 7(c) and 8(c). At the depth of 8 km (Fig. 5e), the low-velocity ($<$3.6 km s^{-1}) can be observed to connect all the volcanic systems, and, therefore, the HT fields too.

It is not unreasonable that all or many of the volcanic systems on the RP may be interconnected, as they have all erupted during the same rifting episodes over the last 4000 yr, except Fagradalsfjall (Sæmundsson *et al.* 2020). The Sæmundsson *et al.* (2020) dating of Holocene lava flows has shown that during rifting episodes over the last 4000 yr, the volcanic activity has affected each system individually, with the activity jumping successively from east to west. Furthermore, Flóvenz *et al.* (2022) suggest that geothermal fluids can move along the BDT zone between HT fields, and elevated seismicity in one RP volcanic system also affects the other systems (Sigmundsson *et al.* 2022).

7.5 The Moho discontinuity

The Moho is the boundary between the crust and the mantle of the Earth. It is estimated to be at a depth of around 8–20 km below the RP, most likely at 15 km depth (e.g. Weir *et al.* 2001; Jacoby *et al.* 2007). Below the Moho depth, the shear wave velocity is almost constant and estimated to be around 4.3–4.5 km s^{-1}. Looking at the vertical cross sections of Figs 6–9, we see an almost constant velocity below 15 km depth. Assuming a velocity of 4.3 km s^{-1} around the depth of the Moho, the Moho depth appears to vary a bit in the study area but can approximately be considered to be at a depth of 15 km.

7.6 Qualitative comparison of shear wave and electrical resistivity images

Finally, we compare our shear wave images below the Krýsuvík and the Reykjanes HT geothermal fields with electrical resistivity images obtained in two recent studies (Hersir *et al.* 2020a; Karlsdóttir *et al.* 2020). A clear (qualitative) correlation between low shear wave velocities and low resistivities in the uppermost 2–3 km can be observed (Figs 10a–d and 11a, b). Interestingly, a similar structure can be inferred from both the resistivity and seismic images, that is some sort of up-doming from 4–6 km depth to 1–2 km depth (Figs 10a, c and 11a, b). Both methods likely reflect a heat up-flow, although they map different physical parameters. Our seismic results are smoother and provide less detail, particularly in the top 2 km. This is inherent to the adopted probabilistic method, the chosen ray-based traveltime approach, and the frequencies of the surface waves we used in this study, which are limited to 0.1–0.5 Hz. Still, the shear wave velocities are low and show a weak up-doming in agreement with the up-doming shallow low resistivity. As we discussed in Fig. 3, our data are mostly sensitive to shear wave velocities at depths between 3 and 8 km. For a higher resolution and hence more details of the top 2 km of the subsurface, higher frequency surface waves would need to be included in our probabilistic inversion. At higher frequencies, residual timing errors and interference from higher modes prevented us from identifying reliable phase velocities for the fundamental mode. Nevertheless, the electrical resistivity cross-sections and the corresponding shear wave velocity cross-sections appear to be roughly consistent with each other, showing similar broad features.

Fig. 10(a) shows well the up-doming of the low resistivity at 6–9 km along the cross-section well with the up-doming of low-velocities on Fig. 10(c), as well as the high resistivity captured by higher shear waves speeds. Fig. 10(b) is simpler, here it is more clear that the central up-doming of low resistivity (at 5–7 km distance along the cross-section) can be associated with up-doming of lower-velocities in Fig. 10(d) at the same location. It should be noted

that the 3-D resistivity models are somewhat non-unique. It is, however, encouraging that the two different geophysical approaches give comparable results. Sánchez-Pastor *et al.* (2021) also observed a correlation between resistivity and shear wave velocity within the Hengill HT geothermal field. The added benefit of this study is that it covers a large area, the entire RP, and has a larger depth of investigation. It can, therefore, give good first indications on where to find geothermal heat up-flow.

Fig. 11(a) shows a resistivity profile transecting the Reykjanes volcanic system, taken from Karlsdóttir *et al.* (2020). The corresponding shear wave velocity profile is shown in Fig. 11(b). A good (qualitative) correlation between the low-velocities and the resistivity structure is observed. Similar to Fig. 10, the shear wave velocity profiles are smoother than the resistivity profiles but still capture the up-doming of the low shear wave velocity, with higher resistivity and higher shear wave velocities on either side.

8 CONCLUSION

We used ambient noise cross-correlations between 79 seismic stations from the extended IMAGE seismic network on- and off-shore the RP to obtain a (relatively) high-resolution shear wave velocity model of the RP. Actually, this is the first tomographic model of the whole RP which is based on both on- and off-shore seismic stations. We first extracted fundamental mode phase velocity dispersion curves using (frequency-dependent) phase traveltimes in the frequency range of 0.1–0.5 Hz, resulting in the best-resolved depths at 2–8 km depth. Subsequently, we used a recently developed one-step transdimensional McMC algorithm to recover the posterior probability distribution of the possible 3-D shear wave velocity models. In general, we observe that the velocity increases from the Earth's surface down to 20 km depth of the pointwise averaged shear wave velocity model. At 5–8 km depth, a decrease in velocity is observed, consistent with the BDT on the RP. Moreover, at 7 km depth, all the volcanic systems are on some level connected by a relatively low-velocity anomaly.

Interestingly, the velocity reduction domes up to 3 km depth below all known HT geothermal fields on the RP, that is Reykjanes, Svartsengi and Krýsuvík (Fig. 1). This correlates well with previously recorded up-doming of the BDT below the same HT fields. We suggest that the observed low-velocity anomalies are due to the an-elasticity of the BDT zone, combined with the high temperatures of the HT fields, although some amount of partial melt can not be excluded. The observed low-velocity anomalies below Reykjanes and Eldvörp-Svartsengi are relatively small but still significant, while the low-velocity anomaly below Krýsuvík is much larger. The Krýsuvík low-velocity anomaly extends almost perpendicular to the volcanic system towards the southeast, coinciding with geothermal surface manifestations and the resistivity structure. More interestingly, a low-velocity anomaly is observed at 3–6 km depth about 1 km northwest of the recent Fagradalsfjall eruption site.

The (qualitative) correlation of our recovered shear wave velocities with resistivity studies conducted on the RP, suggests that the one-step transdimensional algorithm has successfully recovered the shear wave velocity structure below the RP. Our shear wave velocity model is smoother and contains fewer details than the recent resistivity studies, especially near the surface (<2 km depth), due to the limited frequency range of the fundamental mode surface waves used, but it captures well the same broad features of the heat up-flow. Considering that this algorithm needs less user-defined (and hence somewhat subjective) parameters, it has great potential to become a routine tool for surface wave seismic tomography.

ACKNOWLEDGMENTS

We would like to thank Ólafur G. Flóvenz and Kristján Ágústsson, former geophysicists at ÍSOR, for helping us interpret the tomographic results at the early stage of writing our paper. We are grateful for the open-access multi-institutional IMAGE data set (Jousset *et al.* 2020a). Especially we want to thank the Institute of Geophysics of the Czech Academy of Science for using the data recorded by the REYKJANET stations, in particular Jakub Klicpera, Bohuslav Růžek and Josef Horálek. Similarly, we thank the Icelandic Meteorological Office (IMO) for providing data. Instruments for the IMAGE project were provided by the GIPP (Geophysical Instrument pool Potsdam) and the DEPAS (German instrument pool for amphibian seismology). We are grateful to the editor and two anonymous reviewers for numerous constructive criticisms of an earlier draft of this paper.

DATA AVAILABILITY

The original MCTomo package for doing the one-step transdimensional tomography algorithm is available here (https://blogs.ed.ac.uk/imaging/research/codes/), which is based on Zhang *et al.* (2018, 2020). However, we have modified the package in two ways. First, we have removed the dependency on external packages like CGAL. Secondly, we update the ray paths less often to make the algorithm computationally less demanding, while at the same time preserving the non-linearity of the solution (see Rahimi Dalkhani *et al.* 2021, for details). The modified package is available upon request. The data underlying this manuscript are published open access (see Rahimi Dalkhani *et al.* 2023). The frequency-dependent Rayleigh wave phase traveltimes (*ttimes.dat*), dispersion curves (*DCs.dat*), location of stations (*sources.dat* & *receivers.dat*) and the input file for running the MCTomo package (*MCTomo.inp*) are accessible at https://doi.org/10.4121/3c97b1c8-1736-495d-a2f9-bd26dc958575. The 3-D posterior mean and uncertainty models and the MATLAB files to regenerate all the figures are also included in the above-mentioned repository. A MATLAB script for retrieving phase velocities from the interferometric responses (Appendix A) is also included.

SUPPORTING INFORMATION

Supplementary data are available at *GJI* online.

suppl_data

Please note: Oxford University Press is not responsible for the content or functionality of any supporting materials supplied by the authors. Any queries (other than missing material) should be directed to the corresponding author for the paper.

REFERENCES

Adelinet, M., Dorbath, C., Le Ravalec, M., Fortin, J. & Guéguen, Y., 2011. Deriving microstructure and fluid state within the Icelandic crust from the inversion of tomography data, *Geophys. Res. Lett.*, **38**(3), doi:10.1029/2010GL046304.

Ágústsdóttir, T. *et al.*, 2023. Relative earthquake relocations and detailed evolution of failed and successful lateral dyke intrusions during the 2021-2022 Fagradalsfjall volcano-tectonic rifting event, in *EGU General Assembly Conference Abstracts,* Vienna, Austria, 24–28 Apr 2023, EGU23-13310.

Ágústsson, K. & Flóvenz, Ó.G., 2005. The thickness of the seismogenic crust in Iceland and its implications for geothermal systems, in *Proceedings of the World Geothermal Congress,* pp. 24–29.

Allen, R.M. *et al.*, 2002. Plume-driven plumbing and crustal formation in Iceland, *J. geophys. Res,* **107**(B8), ESE 4–1-ESE 4-19.

Árnason, K., 2020. New conceptual model for the magma-hydrothermal-tectonic system of Krafla, NE Iceland, *Geosciences,* **10**(1), doi:10.3390/geosciences10010034.

Árnason, K., Eysteinsson, H. & Hersir, G.P., 2010. Joint 1D inversion of TEM and MT data and 3D inversion of MT data in the Hengill area, SW Iceland, *Geothermics,* **39**(1), 13–34.

Arnórsson, S., 1987. Gas chemistry of the Krísuvík geothermal field, Iceland, with special reference to evaluation of steam condensation in upflow zones, *Jökull,* (37), 31–48.

Arnórsson, S., Björnsson, A., Gíslason, G. & Gudmundsson, G., 1976. Systematic exploration of the Krísuvík high-temperature area, Reykjanes Peninsula, Iceland, in *Proceedings of the Second UN Geothermal Symposium,* pp. 853–864.

Bali, E. *et al.*, 2020. Geothermal energy and ore-forming potential of 600 °C mid-ocean-ridge hydrothermal fluids, *Geology,* **48**(12), 1221–1225.

Björnsson, S., Einarsson, P., Tulinius, H. & Hjartardóttir, Á.R., 2020. Seismicity of the Reykjanes Peninsula 1971–1976, *J. Volc. Geotherm. Res.,* **391,** doi:10.1016/j.jvolgeores.2018.04.026.

Blanck, H., Jousset, P., Hersir, G.P., Ágústsson, K. & Flóvenz, Ó.G., 2020. Analysis of 2014–2015 on-and off-shore passive seismic data on the Reykjanes Peninsula, SW Iceland, *J. Volc. Geotherm. Res.,* **391,** doi:10.1016/j.jvolgeores.2019.02.001.

Bodin, T. & Sambridge, M., 2009. Seismic tomography with the reversible jump algorithm, *Geophys. J. Int.,* **178**(3), 1411–1436.

Bodin, T., Sambridge, M. & Gallagher, K., 2009. A self-parametrizing partition model approach to tomographic inverse problem, *Inverse Problem,* **25**(5), doi:10.1088/0266-5611/25/5/055009.

Bodin, T., Sambridge, M., Rawlinson, N. & Arroucau, P., 2012. Transdimensional tomography with unknown data noise, *Geophys. J. Int.,* **189**(3), 1536–1556.

Boschi, L., Weemstra, C., Verbeke, J., Ekstrom, G., Zunino, A. & Giardini, D., 2013. On measuring surface wave phase velocity from station-station cross-correlation of ambient signal, *Geophys. J. Int.,* **192,** 346–358.

Cabrera-Pérez, I., D'Auria, L., Soubestre, J., Barrancos, J., Padilla, G.D. & Pérez, N.M., 2021. A nonlinear multiscale inversion approach for ambient noise tomography, *Geophys. J. Int.,* **225**(2), 1158–1173.

Caracciolo, A., Bali, E., Halldórsson, S., Guðfinnsson, G., Kahl, M., Þórðardóttir, I., Pálmadóttir, G. & Silvestri, V., 2023. Magma plumbing architectures and timescales of magmatic processes during historical magmatism on the Reykjanes Peninsula, Iceland, *Earth planet. Sci. Lett.,* **621,** doi:10.1016/j.epsl.2023.118378.

Chen, X., Zhang, Y., Hui, D., Chen, M. & Wu, Z., 2017. Study of melting properties of basalt based on their mineral components, *Compos. B. Eng.,* **116,** 53–60.

Clifton, A.E. & Kattenhorn, S.A., 2006. Structural architecture of a highly oblique divergent plate boundary segment, *Tectonophysics,* **419**(1-4), 27–40.

Cruz-Hernández, F., Gallardo, L.A., Calò, M., Castro, R.R. & Romo-Jones, J.M., 2022. Ambient noise tomography in the Cerro Prieto Basin, Baja California, Mexico from laterally constrained surface wave inversion, *Geophys. J. Int.,* **229**(3), 1586–1603.

Du, Z. *et al.*, 2002. Crustal structure beneath western and eastern Iceland from surface waves and receiver functions, *Geophys. J. Int.,* **149**(2), 349–363.

Dziewonski, A.M. & Anderson, D.L., 1981. Preliminary reference earth model, *Phys. Earth planet. Inter.,* **25**(4), 297–356.

Einarsson, P., 1991. Earthquakes and present-day tectonism in Iceland, *Tectonophysics,* **189**(1–4), 261–279.

Einarsson, P., Eyjólfsson, V. & Hjartardóttir, Á.R., 2023. Tectonic framework and fault structures in the Fagradalsfjall segment of the Reykjanes Peninsula Oblique Rift, Iceland, *Bull. Volcanol.,* **85**(2), doi:10.1007/s00445-022-01624-x.

Ekström, G., Abers, G. & Webb, S., 2009. Determination of surface-wave phase velocities across USArray from noise and AKI's spectral formulation, *Geophys. Res. Lett.,* **36,** doi:10.1029/2009GL039131.

Fang, H., Yao, H., Zhang, H., Huang, Y.-C. & van der Hilst, R.D., 2015. Direct inversion of surface wave dispersion for three-dimensional shallow crustal structure based on ray tracing: methodology and application, *Geophys. J. Int.,* **201**(3), 1251–1263.

Fischer, T., Hrubcová, P., Salama, A., Doubravová, J., Ágústsdóttir, T., Gudnason, E., Horálek, J. & Hersir, G.P., 2022. Swarm seismicity illuminates stress transfer prior to the 2021 Fagradalsfjall eruption in Iceland, *Earth planet. Sci. Lett.,* **594,** doi:10.1016/j.epsl.2022.117685.

Flóvenz, l.G. *et al.*, 1980. Seismic structure of the Icelandic crust above layer three and the relation between body wave velocity and the alteration of the basaltic crust, *J. Geophys.,* **47**(1), 211–220.

Flóvenz, Ó.G. *et al.*, 2022. Cyclical geothermal unrest as a precursor to Iceland's 2021 Fagradalsfjall eruption, *Nat. Geosci,* **15**(5), 397–404.

Foulger, G., Du, Z. & Julian, B., 2003. Icelandic-type crust, *Geophys. J. Int.,* **155**(2), 567–590.

Friðleifsson, G.Ó. *et al.*, 2020. The Iceland deep drilling project at Reykjanes: drilling into the root zone of a black smoker analog, *J. Volc. Geotherm. Res.,* **391,** doi:10.1016/j.jvolgeores.2018.08.013.

Froment, B., Campillo, M., Roux, P., Gouédard, P., Verdel, A. & Weaver, R.L., 2010. Estimation of the effect of nonisotropically distributed energy on the apparent arrival time in correlations, *Geophysics,* **75,** SA85–SA93.

Galetti, E., Curtis, A., Baptie, B., Jenkins, D. & Nicolson, H., 2017. Transdimensional love-wave tomography of the British Isles and shear-velocity structure of the east Irish Sea Basin from ambient-noise interferometry, *Geophys. J. Int.,* **208**(1), 36–58.

Gelman, A., *et al.*, 1996. Efficient metropolis jumping rules, *Bayesian Stat.,* **5,** 599–607.

Greenfield, T. *et al.*, 2022. Deep long period seismicity preceding and during the 2021 Fagradalsfjall Eruption, Iceland, *Bull. Volcanol.,* **84**(12), 1–20.

Gudnason, E., Köpke, R., Gaucher, E., Ágústsson, K., Níelsson, S. & Kohl, T., 2021. Seismic monitoring during drilling and stimulation of well RN-15/IDDP-2 in Reykjanes, SW Iceland, in *Proceedings of the World Geothermal Congress 2020+1,* Reykjavík, Iceland.

Guðmundsson, M.T., Högnadóttir, Þ. & Háskólans, J., 2004. *Hraun og móbergsmyndanir á svæðinu frá Brennisteinsfjöllum að Hengli: niðurstöður þyngdarmælinga,* Jarðvísindastofnun Háskólans.

Halldórsson, S.A. *et al.*, 2022. Rapid shifting of a deep magmatic source at Fagradalsfjall Volcano, Iceland, *Nature,* **609,** 529–534.

Halliday, D. & Curtis, A., 2008. Seismic interferometry, surface waves and source distribution, *Geophys. J. Int.,* **175,** 1067–1087.

Haney, M., Mikesell, T.D., van Wijk, K. & Nakahara, H., 2012. Extension of the spatial autocorrelation (SPAC) method to mixed-component correlations of surface waves, *Geophys. J. Int.,* **191**(1), 189–206.

Haney, M.M. & Tsai, V.C., 2015. Nonperturbational surface-wave inversion: a dix-type relation for surface waves, *Geophysics,* **80**(6), EN167–EN177.

Herrmann, R.B., 2013. Computer programs in seismology: an evolving tool for instruction and research, *Seismol. Res. Lett.,* **84**(6), 1081–1088.

Hersir, G.P., Björnsson, G. & Björnsson, A., 1990. *Eldstöðvar og jarðhiti á hengilssvæðinu: jarðeðlisfræðileg könnun. orkustofnun,* Tech. rep., OS-90031/JHD-06.

Hersir, G.P., Árnason, K., Vilhjálmsson, A.M., Saemundsson, K., Ágústsdóttir, Þ. & Friðleifsson, G.Ó., 2020. Krýsuvík high temperature geothermal area in SW Iceland: Geological setting and 3D inversion of magnetotelluric (MT) resistivity data, *J. Volc. Geotherm. Res.,* **391,** doi:10.1016/j.jvolgeores.2018.11.021.

Hersir, G.P., Flóvenz, Ó.G., Bruhn, D., Liotta, D., van Wees, J.-D., Halldórsdóttir, S. & Manzella, A., 2021. Geothermal exploration and reservoir assessment in magmatic systems the image project, in *Proceedings World Geothermal Congress2020+1,*Reykjavík, Iceland.

Hobé, A., Gudmundsson, O., Tryggvason, A. *et al.*, 2021. Imaging the 2010-2011 inflationary source at Krysuvik, SW Iceland, using time-dependent

Vp/Vs tomography, in *World Geothermal Congress 2020+1,* Reykjavík, Iceland.
Horálek, J., 2013. *Reykjanet [2014-2015] [Data set]. International Federation of Digital Seismograph Networks,* doi:10.7914/SN/7E_2013.
Icelandic Meteorological Office, 1992. Icelandic National Digital Seismograph Network [Data set]. International Federation of Digital Seismograph Networks. https://doi.org/10.7914/zkjm-tj71.
Jacoby, W.R., Weigel, W. & Fedorova, T., 2007. Crustal structure of the Reykjanes Ridge near 62°N, on the basis of seismic refraction and gravity data, *J. Geodyn.,* **43**(1), 55–72.
Jakobsdóttir, S.S., 2008. Seismicity in Iceland: 1994–2007, *Jökull,* **58**(1), 75–100.
Jousset, P. *et al.*, 2016. Seismic tomography in Reykjanes, SW Iceland, in *European Geothermal Congress 2016, Extended Abstract ,* Strasbourg, France.
Jousset, P. *et al.*, 2020a. *IMAGE (Integrated Methods for Advanced Geothermal Exploration),* doi:10.14470/9Y7569325908.
Jousset, P., Mortensen, A.K., Fridleifsson, G.Ó., Ágústsson, K. & Gudmundsson, M.T., 2020b. Reykjanes, Iceland: structure and dynamics of mid-oceanic ridge geo/hydrothermal systems, *J. Volc. Geotherm. Res.,* **391,** doi:10.1016/j.jvolgeores.2019.106692.
Karato, S.-I., 2014. Does partial melting explain geophysical anomalies?, *Phys. Earth planet. Inter.,* **228,** 300–306.
Karlsdóttir, R., Vilhjálmsson, A.M. & Guðnason, E.Á., 2020. Three dimensional inversion of magnetotelluric (MT) resistivity data from Reykjanes high temperature field in SW Iceland, *J. Volc. Geotherm. Res.,* **391,** doi:10.1016/j.jvolgeores.2018.11.019.
Kästle, E.D., Soomro, R., Weemstra, C., Boschi, L. & Meier, T., 2016. Two-receiver measurements of phase velocity: cross-validation of ambient-noise and earthquake-based observations, *Geophys. J. Int.,* **207**(3), 1493–1512.
Khodayar, M., Björnsson, S., Guðnason, E.Á., Níelsson, S., Axelsson, G. & Hickson, C., 2018. Tectonic control of the Reykjanes geothermal field in the oblique rift of SW Iceland: from regional to reservoir scales, *Open J. Geol.,* **8**(3), 333–382.
Kurita, T., 1973. Regional variations in the structure of the crust in the central united states from P-wave spectra, *Bull. seism. Soc. Am.,* **63**(5), 1663–1687.
Lees, J.M., 2007. Seismic tomography of magmatic systems, *J. Volc. Geotherm. Res.,* **167**(1–4), 37–56.
Lehujeur, M., Vergne, J., Maggi, A. & Schmittbuhl, J., 2016. Ambient noise tomography with non-uniform noise sources and low aperture networks: case study of deep geothermal reservoirs in Northern Alsace, France, *Mon. Not. R. astr. Soc.,* **208**(1), 193–210.
Lehujeur, M., Chevrot, S., Villaseñor, A., Masini, E., Saspiturry, N., Lescoutre, R. & Sylvander, M., 2021. Three-dimensional shear velocity structure of the Mauléon and Arzacq Basins (Western Pyrenees), *Bull. Soc. géol. Fr.,* **192**(1), doi:10.1051/bsgf/2021039.
Lindner, F., Weemstra, C., Walter, F. & Hadziioannou, C., 2018. Towards monitoring the englacial fracture state using virtual-reflector seismology, *Geophys. J. Int.,* **214**(2), 825–844.
Martins, J.E., Weemstra, C., Ruigrok, E., Verdel, A., Jousset, P. & Hersir, G.P., 2020. 3D S-wave velocity imaging of Reykjanes Peninsula high-enthalpy geothermal fields with ambient-noise tomography, *J. Volc. Geotherm. Res.,* **391,** doi:10.1016/j.jvolgeores.2019.106685.
McKenzie, D., 2000. Constraints on melt generation and transport from u-series activity ratios, *Chem. Geol.,* **162**(2), 81–94.
Michalczewska, K. *et al.*, 2012. Inflation and deflation episodes in the Krýsuvík Volcanic System, in *American Geophysical Union, Fall Meeting 2012,* abstract id. V33A-2843.
Obermann, A. *et al.*, 2022. Seismicity and 3-D body-wave velocity models across the Hengill Geothermal Area, SW Iceland, *Front. Earth Sci.,* **10,** doi:10.3389/feart.2022.969836.
Pálmason, G., 1971. Crustal structure of Iceland from explosion seismology, Prentsmithjan Leiftur Reykjavik.
Pedersen, G.B. *et al.*, 2022. Volume, effusion rate, and lava transport during the 2021 Fagradalsfjall eruption: results from near real-time photogrammetric monitoring, *Geophys. Res. Lett.,* **49**(13), e2021GL097125.
Priestley, K. & McKenzie, D., 2006. The thermal structure of the lithosphere from shear wave velocities, *Earth planet. Sci. Lett.,* **244**(1–2), 285–301.
Priestley, K. & McKenzie, D., 2013. The relationship between shear wave velocity, temperature, attenuation and viscosity in the shallow part of the mantle, *Earth planet. Sci. Lett.,* **381,** 78–91.
Rahimi Dalkhani, A., Zhang, X. & Weemstra, C., 2021. On the potential of 3D transdimensional surface wave tomography for geothermal prospecting of the Reykjanes Peninsula, *Remote Sens.,* **13**(23), doi:10.3390/rs13234929.
Rahimi Dalkhani, A., Ágústsdóttir, T., Gudnason, E.Á., Hersir, G.P., Zhang, X. & Weemstra, C., 2023. Data underlying the publication: Transdimensional ambient-noise surface wave tomography of the Reykjanes Peninsula, SW Iceland, 4TU.ResearchData, Dataset, doi: 10.4121/3c97b1c8-1736-495d-a2f9-bd26dc958575.
Rawlinson, N. & Sambridge, M., 2004. Wave front evolution in strongly heterogeneous layered media using the fast marching method, *Geophys. J. Int.,* **156**(3), 631–647.
Rawlinson, N., Sambridge, M. *et al.*, 2003. Seismic traveltime tomography of the crust and lithosphere, *Adv. Geophys.,* **46,** 81–199.
Sæmundsson, K. & Sigurgeirsson, M., 2013. Reykjanesskagi, in *Náttúruvá á Íslandi. Eldgos og Jarðskjálftar,* pp. 379–401, ed. Sólnes, J., Viðlagatrygging Íslands/Háskólaútgáfan.
Sæmundsson, K., Sigurgeirsson, M.Á. & Friðleifsson, G.Ó., 2020. Geology and structure of the Reykjanes Volcanic System, Iceland, *J. Volc. Geotherm. Res.,* **391,** doi:10.1016/j.jvolgeores.2018.11.022.
Sánchez-Pastor, P. *et al.*, 2021. Imaging high-temperature geothermal reservoirs with ambient seismic noise tomography, a case study of the Hengill Geothermal Field, SW Iceland, *Geothermics,* **96,** doi:10.1016/j.geothermics.2021.102207.
Saygin, E. & Kennett, B., 2012. Crustal structure of Australia from ambient seismic noise tomography, *J. geophys. Res,* **117**(B1), doi:10.1029/2011JB008403.
Schippkus, S., Zigone, D., Bokelmann, G., Group, A.W. *et al.*, 2018. Ambient-noise tomography of the wider Vienna Basin Region, *Geophys. J. Int.,* **215**(1), 102–117.
Shapiro, N.M. & Campillo, M., 2004. Emergence of broadband Rayleigh waves from correlations of the ambient seismic noise, *Geophys. Res. Lett.,* **31**(7), doi:10.1029/2004GL019491.
Sigmundsson, F. *et al.*, 2020. Geodynamics of Iceland and the signatures of plate spreading, *J. Volc. Geotherm. Res.,* **391,** doi:10.1016/j.jvolgeores.2018.08.014.
Sigmundsson, F. *et al.*, 2022. Deformation and seismicity decline before the 2021 Fagradalsfjall eruption, *Nature,* **609,** 523–528.
Takei, Y., 2017. Effects of partial melting on seismic velocity and attenuation: a new insight from experiments, *Annu. Rev. Earth planet. Sci.,* **45,** 447–470.
Tryggvason, A., Rögnvaldsson, S.T. & Flóvenz, O.G., 2002. Three-dimensional imaging of the P- and S-wave velocity structure and earthquake locations beneath southwest Iceland, *Geophys. J. Int.,* **151**(3), 848–866.
Tsai, V.C., 2009. On establishing the accuracy of noise tomography travel-time measurements in a realistic medium, *Geophys. J. Int.,* **178,** 1555–1564.
Verdel, A. *et al.*, 2016. Reykjanes ambient noise reflection interferometry, in *Proceedings of the European Geothermal Congress,* Strasbourg, France.
Violay, M., Gibert, B., Mainprice, D., Evans, B., Dautria, J.-M., Azais, P. & Pezard, P., 2012. An experimental study of the brittle-ductile transition of basalt at oceanic crust pressure and temperature conditions, *J. geophys. Res,* **117**(B3), doi:10.1029/2011JB008884.
Wapenaar, K. & Fokkema, J., 2006. Green's function representations for seismic interferometry, *Geophysics,* **71**(4), SI33–SI46.
Weaver, R., Froment, B. & Campillo, M., 2009. On the correlation of non-isotropically distributed ballistic scalar diffuse waves., *J. acoust. Soc. Am.,* **126,** 1817–1826.
Weemstra, C., Boschi, L., Goertz, A. & Artman, B., 2013. Seismic attenuation from recordings of ambient noise, *Geophysics,* **78,** Q1–Q14.

Weemstra, C., Westra, W., Snieder, R. & Boschi, L., 2014. On estimating attenuation from the amplitude of the spectrally whitened ambient seismic field, *Geophys. J. Int.,* **197,** 1770–1788.

Weemstra, C., Snieder, R. & Boschi, L., 2015. On the estimation of attenuation from the ambient seismic field: inferences from distributions of isotropic point scatterers, *Geophys. J. Int.,* **203,** 1054–1071.

Weemstra, C. *et al.*, 2016. Time-lapse seismic imaging of the Reykjanes geothermal reservoir, in *Proceedings of the European Geothermal Congress,* Strasbourg, France.

Weemstra, C., De Laat, J.I., Verdel, A. & Smets, P., 2021. Systematic recovery of instrumental timing and phase errors using interferometric surface-waves retrieved from large-n seismic arrays, *Geophys. J. Int.,* **224**(2), 1028–1055.

Weir, N.R., White, R.S., Brandsdóttir, B., Einarsson, P., Shimamura, H. & Shiobara, H., 2001. Crustal structure of the northern Reykjanes Ridge and Reykjanes Peninsula, Southwest Iceland, *J. geophys. Res.,* **106**(B4), 6347–6368.

Xia, J., Miller, R.D. & Park, C.B., 1999. Estimation of near-surface shear-wave velocity by inversion of Rayleigh waves, *Geophysics,* **64**(3), 691–700.

Yao, H., van Der Hilst, R.D. & De Hoop, M.V., 2006. Surface-wave array tomography in SE Tibet from ambient seismic noise and two-station analysis—I. Phase velocity maps, *Geophys. J. Int.,* **166**(2), 732–744.

Yao, H., Beghein, C. & Van Der Hilst, R.D., 2008. Surface wave array tomography in SE Tibet from ambient seismic noise and two-station analysis—II. Crustal and upper-mantle structure, *Geophys. J. Int.,* **173**(1), 205–219.

Zhang, X., Curtis, A., Galetti, E. & De Ridder, S., 2018. 3-D Monte Carlo surface wave tomography, *Geophys. J. Int.,* **215**(3), 1644–1658.

Zhang, X., Hansteen, F., Curtis, A. & De Ridder, S., 2020. 1-D, 2-D, and 3-D Monte Carlo ambient noise tomography using a dense passive seismic array installed on the North Sea seabed, *J. geophys. Res,* **125**(2), e2019JB018552.

APPENDIX A: RAYLEIGH WAVE PHASE VELOCITY RETRIEVAL

Rayleigh waves are interface waves that travel along the free surface of a solid medium. They become dispersive if the medium's shear wave velocity varies (usually increases) with depth. This dispersive behaviour means that at different frequencies, Rayleigh waves propagate along the Earth's surface at different velocities. In other words, their wave speed is frequency-dependent in a vertically heterogeneous medium. Consequently, each phase reaches the receiver at a different time. Extracting frequency-dependent traveltimes from a set of interferometric surface waves traversing a region, therefore allows one to estimate the shear wave velocity structure of that region.

The theory underlying seismic interferometry predicts that time-averaged cross-correlations of long recordings of ambient seismic noise may coincide with the surface wave part of the medium's Green's function (Wapenaar & Fokkema 2006). This implies that these cross-correlation functions can be used to extract frequency-dependent phase or group traveltimes. These traveltimes may subsequently be used to solve a tomographic inverse problem, resulting in 3-D shear wave velocity images of the subsurface. This has been demonstrated at various scales and in different contexts (Shapiro & Campillo 2004; Weemstra *et al.* 2013). At the same time, the limitations have also been pointed out by various authors (e.g. Weaver *et al.* 2009; Tsai 2009). For a detailed derivation of the relation between the surface wave Green's function and the time-averaged cross-correlation, including underlying assumptions and limitations, we, therefore, refer to Halliday & Curtis (2008).

Assuming a lossless, laterally invariant subsurface, and ignoring higher order modes (i.e. only considering the fundamental mode), the real part of the surface wave Green's function (frequency-domain representation) coincides with a zeroth order Bessel function of the first kind [$J_0(\alpha)$; e.g. Boschi *et al.* 2013]. Here,

$$\alpha = \frac{2\pi * f * r}{c(f)}, \tag{A1}$$

where f is frequency, r the station–station distance and $c(f)$ the (Rayleigh wave) phase velocity at frequency f. The latter function is the sought-for phase velocity dispersion curve. The above implies that the dispersive character of the medium between two specific stations, which are separated by a distance r, can be estimated by equating the zeros of the real part of the time-averaged cross-correlation to the zeros of $J_0(\alpha)$. Because the amplitudes of interferometric surface wave responses may suffer from both processing artefacts and violated conditions, equating the zeros is preferred over equating the real part in its entirety (Ekström *et al.* 2009; Weemstra *et al.* 2014, 2015).

For a specific station couple separated by distance r, the (average) phase velocity along the ray connecting the two stations is estimated as follows. At each frequency f for which the real part of the cross-spectrum coincides with zero, a set of candidate phase velocities $c_j(f)$ ($j = 1, 2,...$) exists. These c_j are obtained by equating the zeros of $J_0(2\pi fr/c(f))$, for all $c(f)$, to the cross-spectrum's zeros. This is done for each zero separately. Fig. A1 illustrates this process for three different station couples. The top row depicts the computed time-averaged cross-correlations. The middle row presents the real part of the cross-spectrum, which is interpolated using cubic splines, where the zeros are represented as solid red dots. For each zero, the different candidate phase velocities c_j are shown as open blue circles in the bottom row.

After calculating the candidate phase velocities for each station couple and zero, the next step is to determine the set of phase velocities (i.e. the non-interpolated dispersion curve) that best represents the true phase velocities. To that end, surface wave dispersion associated with a reference model is often used (for example the preliminary reference Earth model PREM; Dziewonski & Anderson 1981). This curve (yellow line in Fig. A1) is used to identify the start of the dispersion curve at the lower end of the spectrum, such as 0.05–0.2 Hz. At higher frequencies, the reference curve flattens out because the PREM does not account for (small-scale) near-surface structure. By imposing a constraint that our picked curve should be continuous, we stop the picking process at the frequency where there is a jump or discontinuity in phase velocity between adjacent frequencies. (For details regarding the picking algorithm we refer to Kästle *et al.* 2016). The rationale behind this is the following: the signal-to-noise ratio (SNR) of the interferometric surface waves decreases with increasing frequency, which may result in such jumps. This decrease in SNR with increasing frequency can be due to (i) stronger attenuation at higher frequencies, (ii) stronger scattering at higher frequencies (and hence a less pronounced ballistic surface wave), (iii) cross-modal terms (Halliday & Curtis 2008) or (iv) a combination of these.

The solid blue circles in the bottom row of Fig. A1 are the picked phase velocities. By means of a cubic spline algorithm, we interpolate those points to obtain phase velocities at an *a priori* defined set of discrete frequencies f_i ($i = 1, 2,...$). The latter is the same for each station couple and hence facilitates a tomographic inversion. The interpolation result is the red line; red plus signs indicate

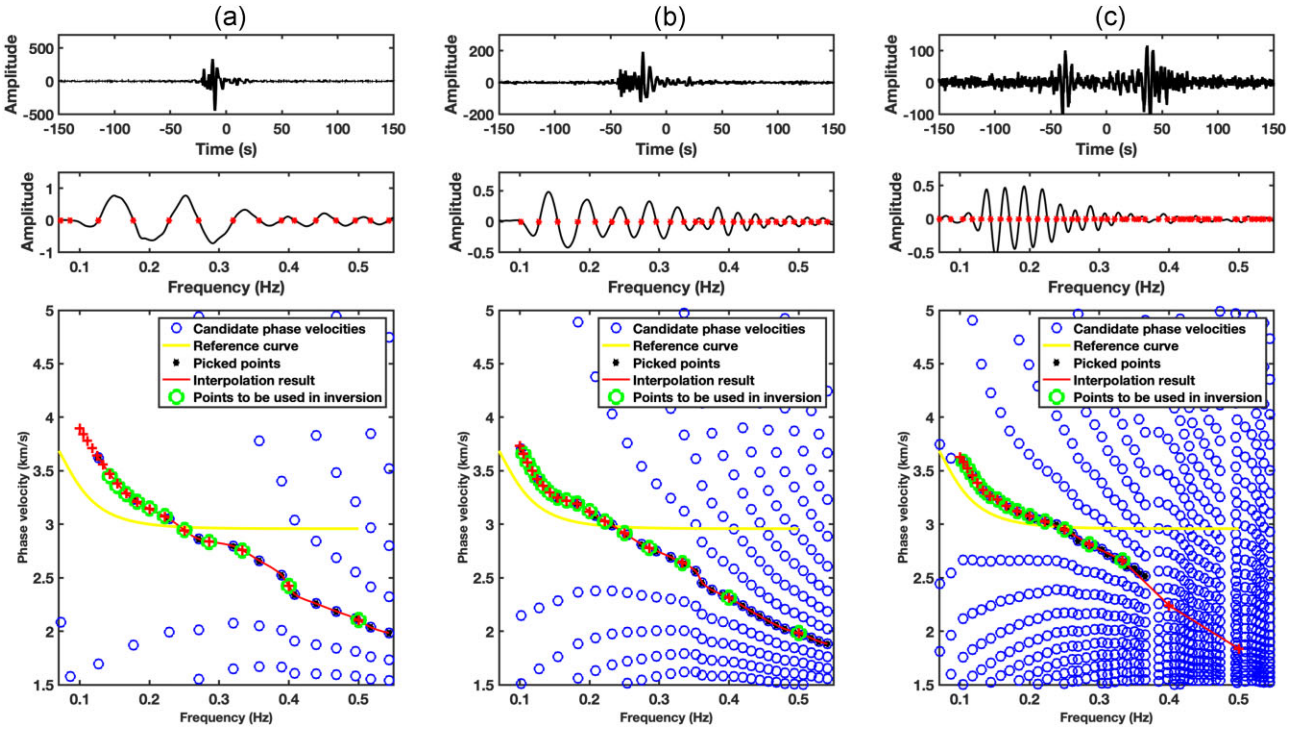

Figure A1. Examples of picked phase velocities for three station couples with station–station distances of (a) 25.1 km, (b) 50 km and (c) 99 km. The top row shows the time-averaged cross-correlation of the corresponding station couple filtered between 0.1 and 0.5 Hz. The middle row shows the real part of the cross-spectrum, interpolated using cubic splines. The bottom row shows candidate phase velocities c_j for each zero (open blue dots). The picked, and subsequently interpolated dispersion curve, is depicted as a red line. The red plus signs depict phase velocities at an *a priori* defined set of frequencies. The corresponding data and codes are accessible in Rahimi Dalkhani *et al.* (2023).

the selected phase velocities at the *a priori* defined frequencies. Importantly, however, not all of these selected phase velocities are deemed reliable. They need to fulfil the criteria that the associated station–station distances exceed one and half a wavelength (at the *a priori* defined frequency). This wavelength is computed using the reference phase velocity curve. For closely separated stations, in particular, this implies that several selected phase velocities at the lower end of the frequency spectrum are discarded. The reason to discard phase velocities associated with closely separated stations (in terms of wavelengths) is that these phase velocities are highly sensitive to deviations from a uniform noise illumination pattern (Weaver *et al.* 2009; Froment *et al.* 2010). Green circles in Fig. A1 show the phase velocities that are deemed reliable and used in the inversion.

APPENDIX B: MODEL UNCERTAINTIES

As we discussed in the text, quantifying solution uncertainties is an advantage of probabilistic inversion algorithms. Here, we present the posterior standard deviation (i.e. a measure of uncertainty) with respect to the posterior means (pointwise average of the retained post-burn-in samples) provided in the body of this article. Figs B1–B5 present the posterior standard deviation with respect to the posterior means presented in Figs 5–9. Fig. B1 shows horizontal slices of the posterior standard deviation at the same depths as Fig. 5, but for the (greater) area that was covered by all stations. Clearly, the uncertainties are lower in the areas that have a high station density (indicated by the black dashed box in Fig. B1). It is the (pointwise) average of the ensemble of shear wave velocities inside this black box that is discussed and (geologically) interpreted in Section 7.

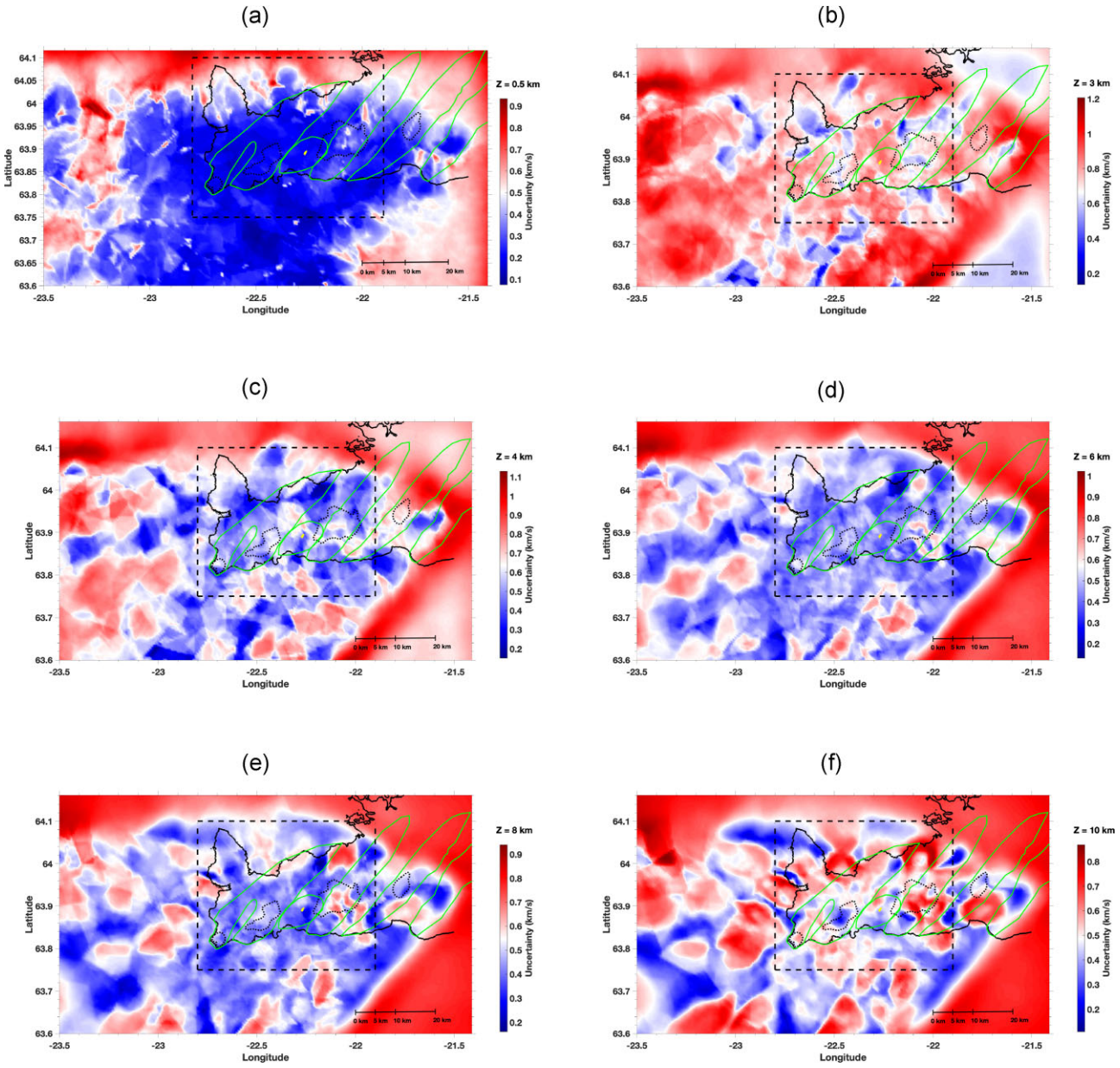

Figure B1. Pointwise standard deviation (from the retained post-burn-in samples) at six different depths: (a) 0.5 km, (b) 3 km, (c) 4 km, (d) 6 km, (e) 8 km and (f) 10 km. The area with the highest resolution and the lowest uncertainties (40 km by 45 km) is indicated by the dashed black box.

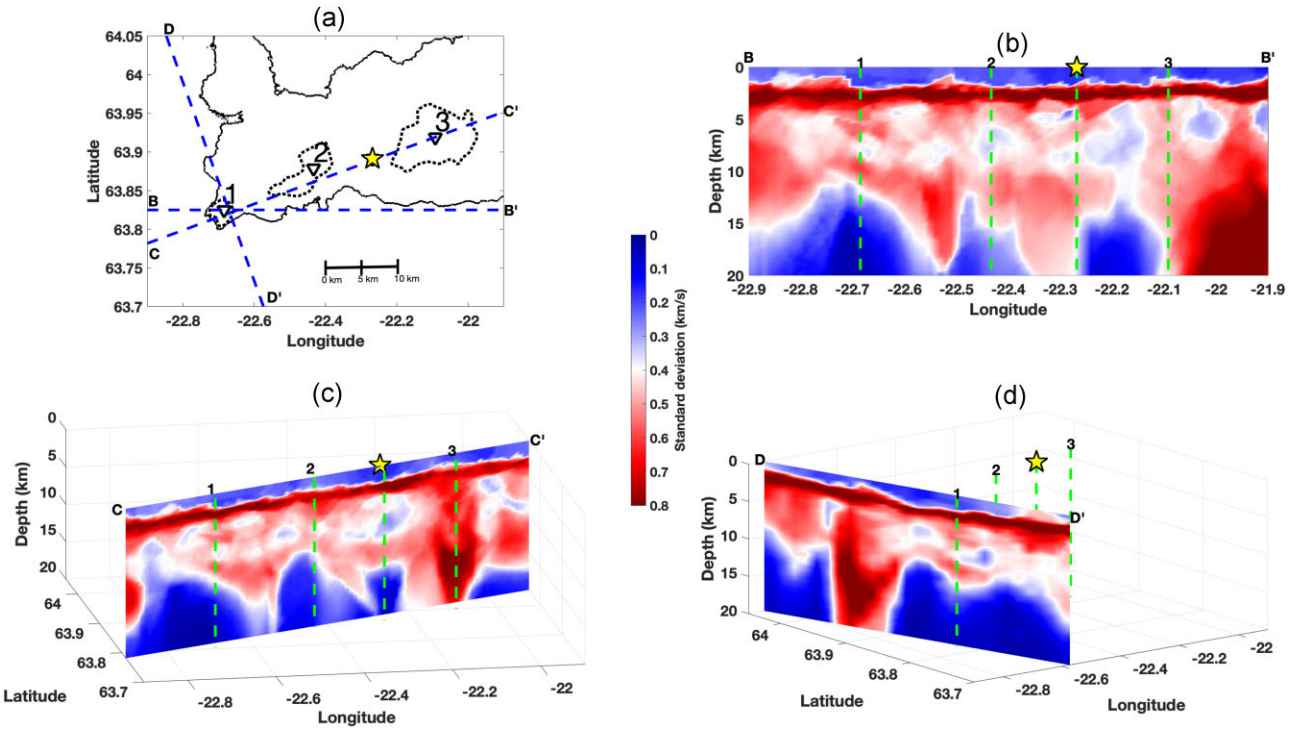

Figure B2. Vertical cross-sections, centred at the location of the Reykjanes HT geothermal field, of the pointwise standard deviation of the retained post-burn-in samples. (a) Map of the area showing the location of three reference points, known high-temperature geothermal fields of Reykjanes, Svartsengi and Krýsuvík (dashed black polygons), blue lines show the locations of the vertical cross-sections of the shear wave velocities along an east-west profile (b), N70°E oriented profile (c) and N20°W oriented profile (d).

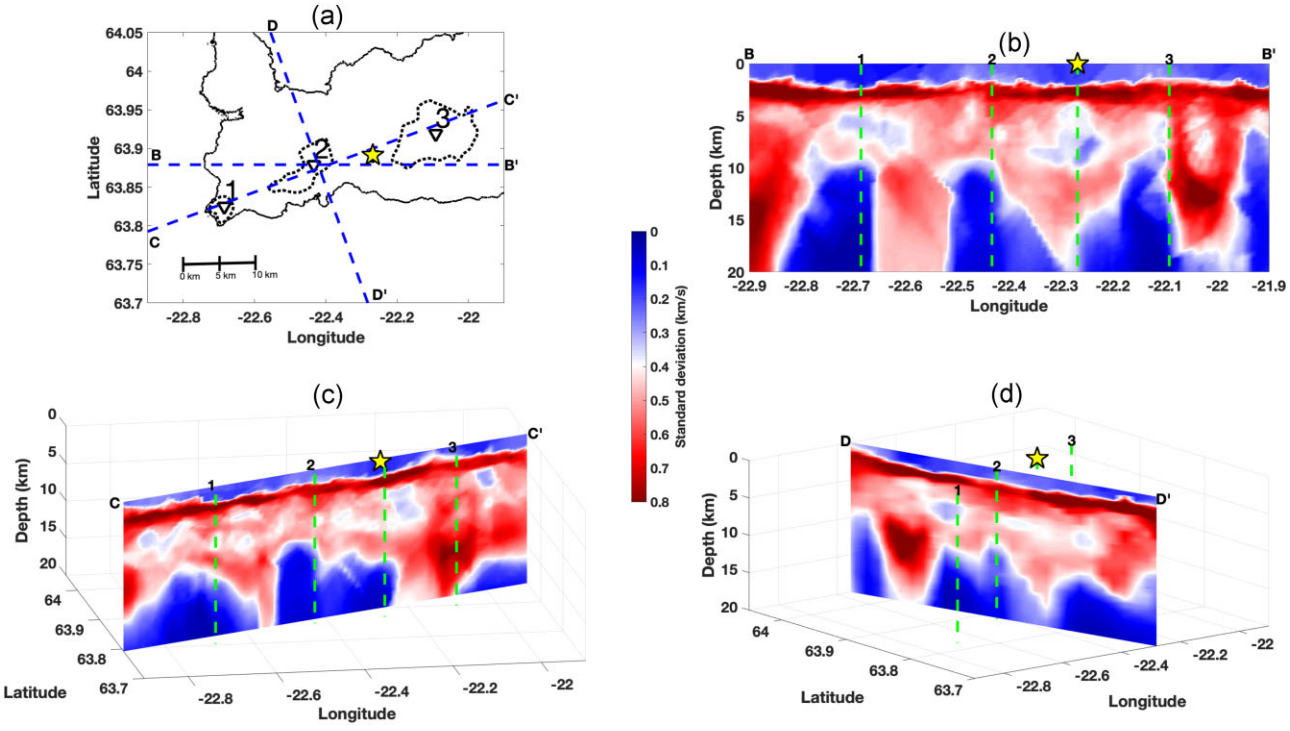

Figure B3. Vertical cross-sections, centred at the location of the Eldvörp-Svartsengi HT geothermal field, of the pointwise standard deviation of the retained post-burn-in samples. (a) Map of the area showing the location of three reference points, known high-temperature geothermal fields of Reykjanes, Svartsengi and Krýsuvík (dashed black polygons), blue lines show the locations of the vertical cross-sections of the shear wave velocities along an east-west profile (b), N70°E oriented profile (c) and N20°W oriented profile (d).

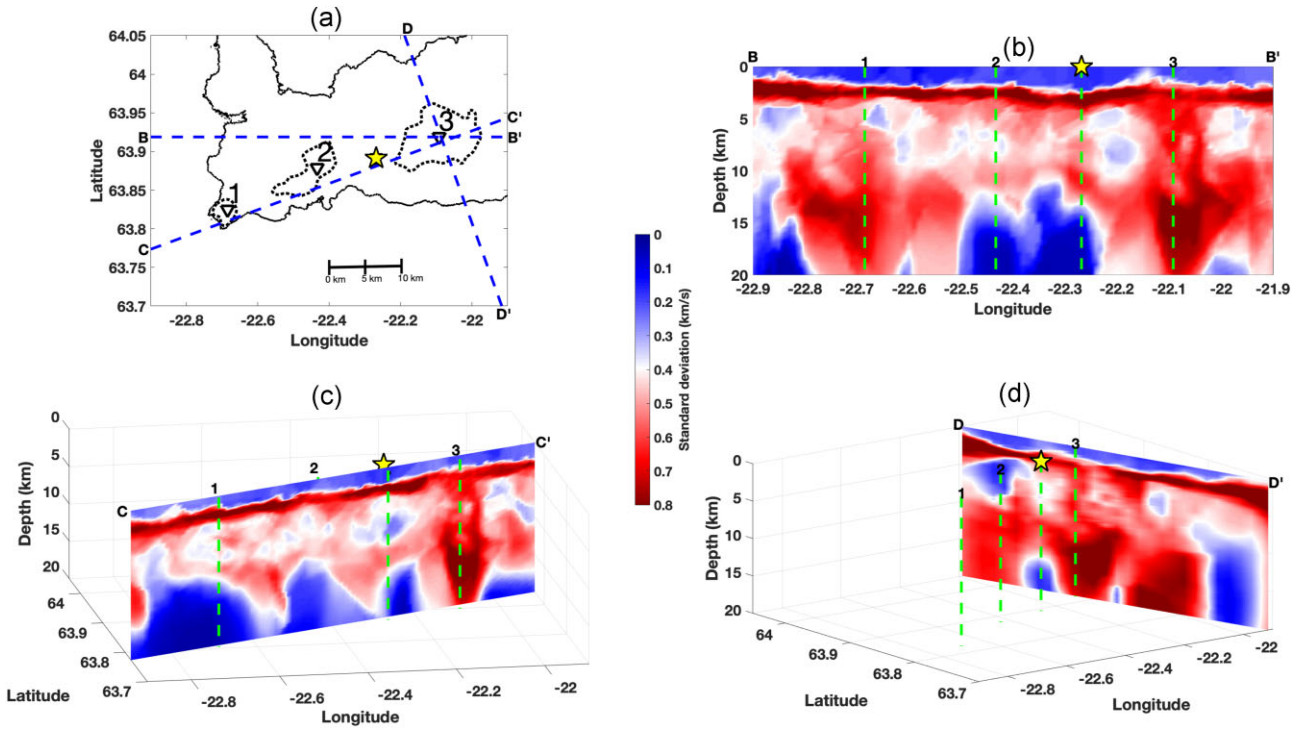

Figure B4. Vertical cross-sections, centred at the location of the Krýsuvík HT geothermal field, of the pointwise standard deviation of the retained post-burn-in samples. (a) Map of the area showing the location of three reference points, known high-temperature geothermal fields of Reykjanes, Svartsengi and Krýsuvík (dashed black polygons), blue lines show the locations of the vertical cross-sections of the shear wave velocities along an east-west profile (b), N70°E oriented profile (c) and N20°W oriented profile (d).

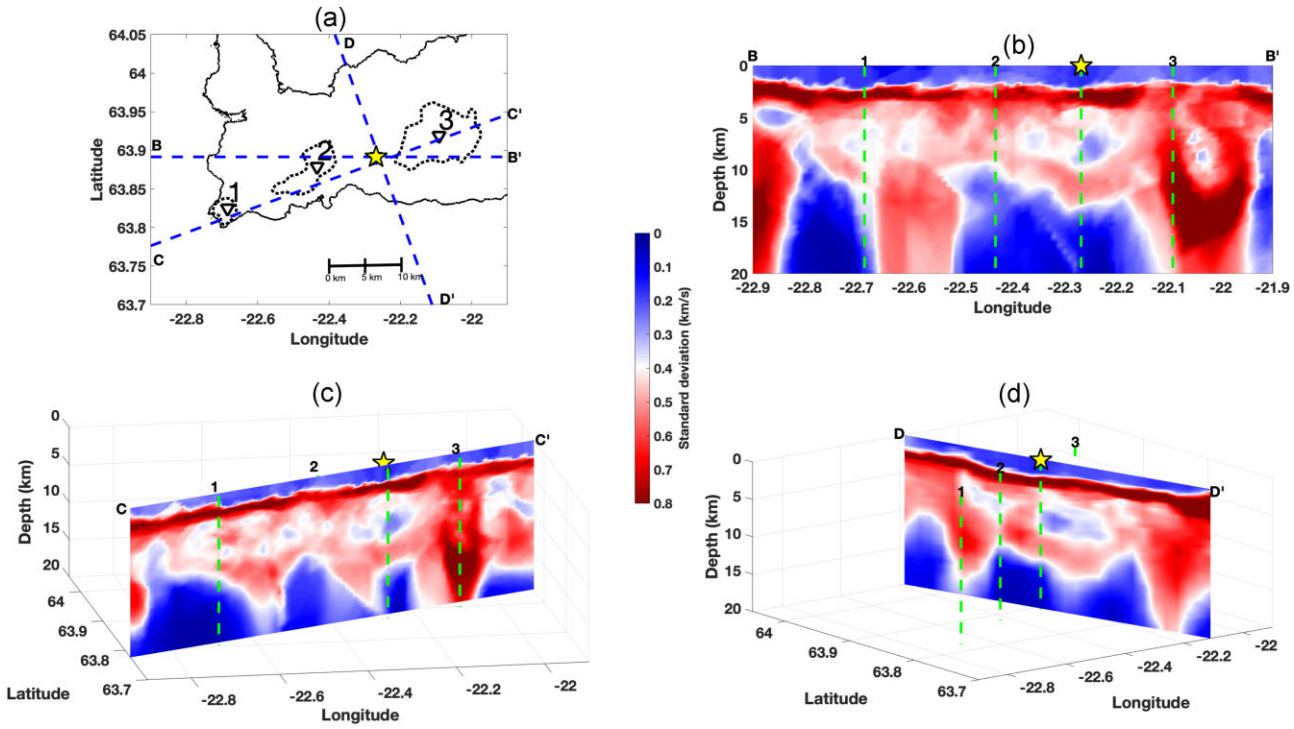

Figure B5. Vertical cross-sections of the pointwise standard deviation, centred at the location of the 2021–2023 eruptions site, on the Fagradalsfjall volcanic system. (a) Map of the area showing the location of three reference points, known high-temperature geothermal fields of Reykjanes, Svartsengi and Krýsuvík (dashed black polygons), blue lines show the locations of the vertical cross-sections of the shear wave velocities along an east-west profile (b), N70°E oriented profile (c) and N20°W oriented profile (d).